Cement and Concrete Research 169 (2023) 107164

Contents lists available at ScienceDirect

Cement and Concrete Research

journal homepage: www.elsevier.com/locate/cemconres

In-situ microtomography image segmentation for characterizing strain-hardening cementitious composites under tension using machine learning

Ke Xu [a,b,*], Qingxu Jin [c,**], Jiaqi Li [d], Daniela M. Ushizima [b,e], Victor C. Li [f], Kimberly E. Kurtis [g], Paulo J.M. Monteiro [a]

[a] Department of Civil and Environmental Engineering, University of California, Berkeley, CA 94720, USA
[b] Computational Research Division, Lawrence Berkeley National Laboratory, Berkeley, CA 94720, USA
[c] Department of Civil and Environmental Engineering, Michigan State University, East Lansing, MI 30332, USA
[d] Atmospheric, Earth, and Energy Division, Lawrence Livermore National Laboratory, 94550, USA
[e] Berkeley Institute for Data Science, University of California, Berkeley, CA 94720, USA
[f] Department of Civil and Environmental Engineering, University of Michigan, Michigan, MI 48109, USA
[g] School of Civil and Environmental Engineering, Georgia Institute of Technology, Atlanta, GA 30332, USA

ARTICLE INFO

Keywords:
Machine learning
Computer vision
Synchrotron microtomography
Image analysis
Strain-hardening cementitious composites
Fiber behavior
Pore structure

ABSTRACT

The application of machine learning and computer vision in microtomography provides new opportunities to directly analyze the microstructural evolutions of strain-hardening cementitious composites (SHCC) under tensile load, especially the strain-hardening process. For the first time, a state-of-the-art machine-learning pipeline combined with digital volume correlation for automated microtomography segmentation analysis (MSA) was developed to separate different components and quantify the in-situ 3D morphological properties of the fibers and pore networks imaged with in-situ synchrotron X-ray computed microtomography. Strain localization and crack initiation were observed around the interconnected pores where strain localized instead of the weakest cross-section defined by the fiber distribution and porosity. Fibers reinforced the crack planes through fiber debonding, bridging, bending, stretching, and orientation redistribution, which contributed to the crack width control and ductility of SHCC in the experiment. This work is essential to understand the progressive damage mechanisms of SHCC and help refine the characterization, modeling, and design of the composite using a bottom-up approach.

1. Introduction

Controlling the crack size in concrete has been one of the greatest challenges in increasing the life cycle of the modern concrete infrastructure [1]. The existing concrete infrastructure is not as durable as desired, although concrete is the most consumed engineered material in the world by mass [2] and is the second most consumed material in the world by mass after water [3]. Cracking is mainly caused by deformation under restraint, mechanical loading and aggressive environmental condition, and crack widths can increase over time with continued loading and environmental exposure.

To improve crack resistance, strain-hardening cementitious composites (SHCC) are being widely studied and show promise for controlling crack width and improving ductility [4–7]. The tensile behavior of SHCC has been extensively studied using conventional mechanical tests over the past decades [8–10]. However, these tests only provide overall material properties (stress/strain) and macro-scale response (fracture pattern) of the material under loading. It is well-known that the microstructural evolution, mainly due to the presence of fibers and fiber orientation, is critical in understanding the tensile behavior of SHCC [11]. In addition, various analytical models have been developed for predicting crack opening and cracking behaviors of SHCC under tension [7,12,13]. These models rely on the morphological and statistical features at the micro-scale, such as statistical assessments of the orientation and distribution of the fibers [14–17].

The traditional methods for assessing the above morphological and

* Correspondence to: K. Xu, Department of Civil and Environmental Engineering, University of California, Berkeley, CA 94720, USA.
** Corresponding author.
E-mail addresses: ke_xu@berkeley.edu (K. Xu), billjin@egr.msu.edu (Q. Jin).

https://doi.org/10.1016/j.cemconres.2023.107164
Received 1 September 2022; Received in revised form 25 January 2023; Accepted 28 March 2023
0008-8846/© 2023 Elsevier Ltd. All rights reserved.

statistical features are either global or ex-situ [18–22]. State-of-the-art high-resolution X-ray microtomographic (μCT) techniques, and the ability to conduct in-situ mechanical tests, have been used to characterize the evolution of composition and microstructure of various cementitious composites and concretes under load [23–25]. To determine the morphological and statistical features from the volumetric representation, there is a critical need to process the three-dimensional raw microtomography (μCT) image data, classify different components (phases), characterize the morphological properties, and conduct a statistical analysis. As one of the most critical steps, accurate and high-speed μCT segmentation methods are required to enable accurate phase segmentation of fiber, pore, and matrix from the reconstructed μCT tomograms [23,26,27]. However, non-metallic fiber phases (e.g., PVA fiber) share pronounced overlaps of gray value spectra with the pore phase, which restricts the application of traditional segmentation methods [19,26,28].

Machine learning (ML) algorithms combined to computer vision methods have been largely applied to segment different phases in microtomography even when the gray value spectra are mixed [29–31]. Recent studies [25,26,32] have shown that ML algorithms, containing both traditional machine learning and deep learning (DL) can be successfully applied to the segmentation of structures of μCT images of concrete and SHCC. However, DL models require thousands of hours of computation time with the help of high-performance and large-storage graphics processing units (GPUs), to finish the model training and prediction [26,33,34]. In addition, the in-situ μCT with a terabyte (TB) scale of raw images further boosts the computation time. Therefore, no in-situ 3D quantification analysis was conducted in the prior research described above. In comparison, classical ML algorithms require less computation time while achieving moderate segmentation accuracy for an SHCC dataset.

The present paper reports an in-situ microtomography segmentation analysis (MSA) using machine learning algorithms. The main advantage of performing an in-situ microtomography segmentation analysis (MSA) is that, in addition to the direct observation and examination of microstructural evolutions (e.g., pore connectivity, fiber behavior, and crack opening) in strain-hardening cementitious composites (SHCC), the statistical information for pore structure, crack opening, fiber distribution and the fiber orientations can also be extracted from the MSA. Such information can be used to investigate the relationship between mechanical responses (e.g., stress/strain and fracture pattern) and microstructural phase information, especially useful for generating correlations between failure patterns and the pore and fiber phases.

There is a consensus that pore structures and fiber behavior influence the tensile properties of SHCC. Researchers [35,36] have observed that the tensile properties of SHCC, in terms of strain capacity and average crack width, are primarily affected by fiber properties, such as fiber orientation, distribution, number of bridging fibers, and fracture ratio, in addition to the fiber/matrix interfacial properties. At the same time, pore structures such as pore volume, pore size distribution, and pore connectivity, influenced by the matrix, aggregates, and fibers in the SHCC, are considered in determining the weakest location (region of crack initiation) and failure mechanism [37–39]. However, above macro-scale or ex-situ micro-scale experiments only provided a limited understanding of the failure mechanism. SHCC samples with the same mixture design can have varied tensile properties due to their heterogeneous nature (e.g., fiber dispersion and orientation, matrix microstructure, and variation of fiber/matrix interface properties).

This paper provides non-destructive in-situ 3D observation and quantitative analysis provided by in-situ MSA at a microstructural scale. 3D pore structures (e.g., porosity, pore connectivity, and pore size distribution) and 3D fiber behavior (e.g., fiber bridging, fiber pull-out, fiber fracture, fiber distribution, and fiber orientation) were characterized and analyzed at different load stages for SHCC sample. Understanding the mechanical responses and failure mechanisms from the microstructural scale can also contribute to the further development of SHCC.

Table 1
Mixture proportion of SHCC (mass ratio).

Cement	Fly ash	Silica sand	w/s	PVA fiber (vol%)
1	1.2	0.8	0.2	2

Table 2
Fiber properties.

Fibers	Diameter	Length	Strength	Young's modulus	Elongation
PVA	39 μm	8 mm	1600 MPa	42.8 GPa	6%

Table 3
Chemical composition of OPC and FA.

Oxide (%)	OPC	FA
Na_2O	0.09	1.01
MgO	3.27	3.20
Al_2O_3	4.56	20.48
SiO_2	20.92	41.78
P_2O_5	0.07	0.96
SO_3	2.62	1.66
K_2O	0.44	1.14
CaO	63.06	15.00
TiO_2	0.22	1.14
Mn_2O_3	0.03	0.00
Fe_2O_3	3.14	12.32
BaO	0	0.42
SrO	0.04	0.23
Sum	98.46	99.34

Also, this work shows that once microstructural data is obtained, it is possible to reduce the variability of fiber behavior in SHCC, especially when the composite undergoes cracking stages, and enhances the predictability of existing micromechanics-based models. In recent decades, models have been developed to capture the strain capacity and average crack width of SHCC [8–10], but the stochastic nature of the properties of the matrix, fiber, and fiber/matrix interface is assumed based on given probabilistic distributions due to the limited ability to access and characterize the heterogeneous microstructure of SHCC under load [15]. For example, Li et al. [14] have shown that using a stochastic approach by assigning random values of micromechanical parameters to each section of SHCC can help reduce the variability of the composite's tensile behavior. However, it is difficult to capture the sequential nature of the fiber behavior based on the pre-assumed distribution in probabilistic approaches. Therefore, in-situ MSA can provide more precise and time-dependent information on pore structure, fiber distribution, and fiber orientation, enhancing the predictive ability of the existing micromechanics-based model.

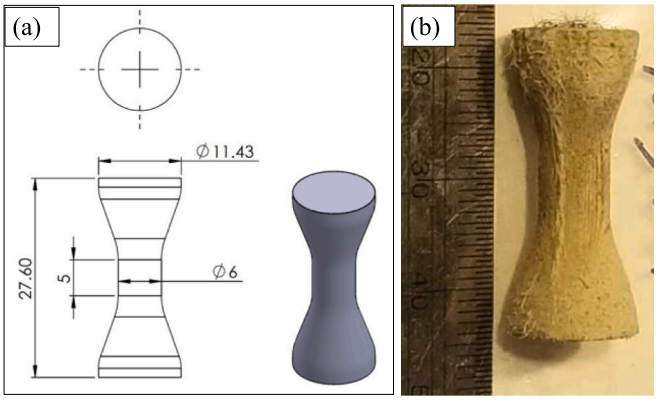

Fig. 1. (a) Specimen details (mm); (b) specimen before in-situ uniaxial tension test. (Image courtesy of Dr. Wilson Nguyen.)

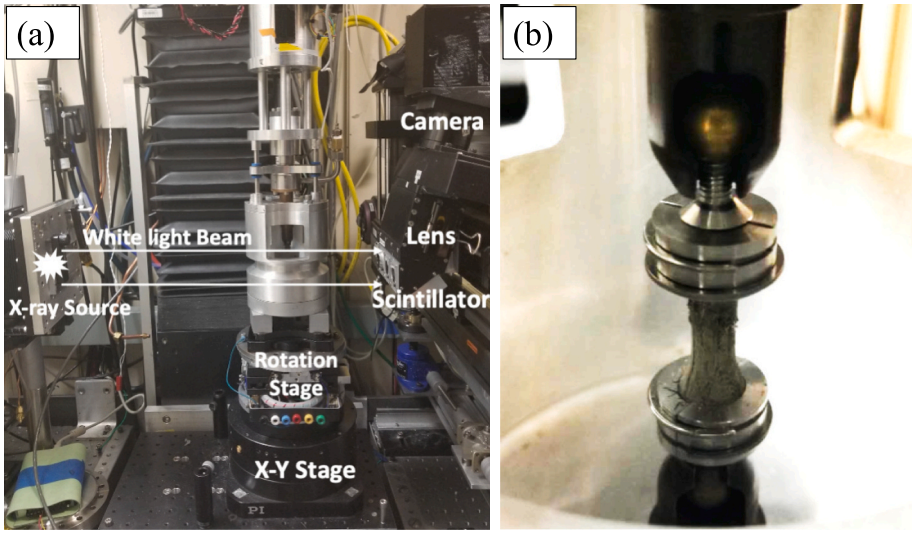

Fig. 2. (a) Global view of in-situ testing apparatus and load chamber installed on the rotation stage of μCT; (b) Interior view of load chamber, showing the tensile specimen with ball and socket connection.

2. Experiments

2.1. Materials and specimen preparation

The SHCC specimens, with mixture proportions given in Table 1, were prepared to analyze fiber behavior and mechanical properties under uniaxial tension. The raw materials used to prepare the SHCC matrix include ASTM C150 Type I/II ordinary Portland cement (OPC, Argos), water, ASTM C618 Class F fly ash (FA, Monroe), and silica sand with D50 of 150 μm. A high-range water reducing admixture (HRWRA, BASF MasterGlenium 3030) was used. Polyvinyl alcohol (PVA) fibers were also used to produce the SHCC, and Table 2 lists their mechanical and geometric properties. The chemical compositions of OPC and FA are given in Table 3, respectively. A 5-L countercurrent mixer (Hobart) was used to mix the SHCC. The fresh SHCC was cast into a 3D-printed mold with a tapered configuration (Fig. 1). The tapered configuration of the SHCC specimen was selected to ensure that a cracked region would develop within the specimen's midheight (the microtomography's field of view) in the uniaxial tension test. A circular cross-section was used to ensure a uniform rotational thickness about the specimen's longitudinal axis and, hence, high-quality microtomography images [40].

After curing for 24 h in the mold while covered with plastic sheeting, the specimens were demolded and cured at 23 ± 2 °C for 28 days before testing. In this study, preliminary tension tests were performed on three samples to assess the mechanical response of the SHCC mix. Another sample was characterized in the in-situ uniaxial tensile tests to study the in-situ microstructural evolutions during the tensioning process. Further details on the sequence of loading and imaging are provided in the Results and discussion section.

2.2. In-situ microtomography (μCT)

The in-situ synchrotron X-ray computed microtomography (μCT) experiments were conducted at the Beamline 8.3.2 of the Advanced Light Source (ALS), Lawrence Berkeley National Laboratory. A white beam with a limited high-penetration X-ray frequency range was used. The beam energy was set to 35 keV with a constant beam current of 500 mA, which is adequate for the penetration of the specimen. For each scan, the specimen was rotated about an axis perpendicular to the horizontal plane over 180° and 1969 2D projections were acquired on a 2560px CCD camera (PCO .edge sCMOS). The exposure time was set at 20 ms to achieve enough contrast.

To characterize the PVA fibers and micro-cracks while achieving an adequate field of view (FOV), a 2x Mitutoyo magnification optical objective lens with a FOV of 4 mm was used. The FOV is constrained by the configuration of the load chamber and testing specimen simultaneously. The regions where the specimen was above the aluminum wall of the light-transparent chamber (Fig. 2b) were not appropriately imaged, limiting the tensile specimen's design length and ROI. The pixel resolution (voxel size) under these conditions was 3.2 μm.

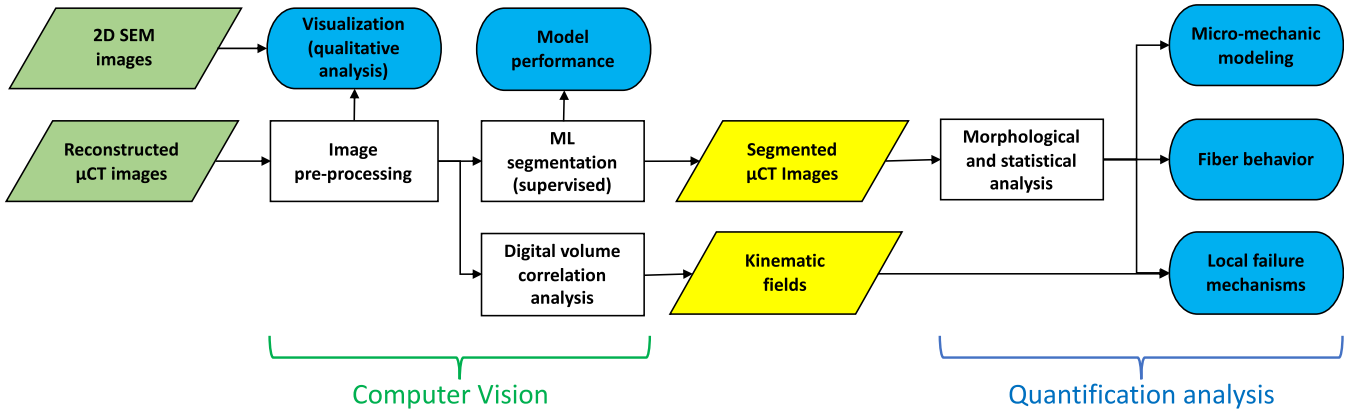

Fig. 3. A schematic diagram showing the stages of machine learning derived in-situ μCT segmentation and analysis.

Reconstructed slices (tomograms) were computed using the filtered back projection algorithm on Tomopy [41,42] at the ALS. After reconstruction, a tomogram of 1200 slices with 2560 × 2560 pixels was obtained for each scan.

The uniaxial tensile loading of the SHCC specimen was done with an existing testing apparatus and load chamber that accommodated the in-situ μCT at ALS (Fig. 2) [23]. Before the experiment, the extremities of the specimen were encased within stainless steel loading heads. The brass spheres attached to the loading heads allowed the specimen to be compatible with the testing apparatus ball and socket connection. Note that this testing setup may produce mechanical slip between components once the load is applied. Therefore, the initial non-linear response of the strain-stress curves was adjusted. The stepper motor applied the tensile load, while the displacement was measured by a linear variable differential transformer (LVDT). The gauge length was 12 mm. The controlled displacement rate in the uniaxial tension experiments was 1 μm/s.

2.3. Scanning electron microscope (SEM) analysis

To understand the fiber bridging behaviors in the SHCC under loading conditions, the fractured cross-sections of the SHCC specimen were studied using a scanning electron microscope (SEM) after the in-situ tensile experiment. The fractured surface of the specimen was gold sputtered. All SEM images were taken under backscattered mode using a Zeiss EVO MA10 microscope. The accelerating voltage and the beam current were 15 kV and 1 nA, respectively. The working distance of the measurements was set to 13.5 – 15 mm.

3. Machine learning-derived image segmentation and quantification analysis

A special data processing pipeline [23,27] (Fig. 3) was developed to systematically investigate the fiber behavior and mechanical properties of tensile SHCC specimens for the autonomous and accurate in-situ μCT image analysis. This pipeline contains two parts: computer vision and statistical analysis. In the computer vision analysis, preprocessed μCT images were segmented into different phases using machine learning (ML) algorithms. The use of edge-preserving filters, mathematical morphology, and an assortment of supervised machine learning algorithms improved the segmentation accuracy. The performances of different ML models were also evaluated. Morphological and statistical analysis was then performed on the in-situ 3D-segmented phase (fiber and pore) images to analyze the time series fiber behavior, pore network, and mechanical properties. The statistical data describing fiber orientation and distribution were examined in the context of mechanical performance using existing micro-mechanic modeling. In addition, advanced digital volume correlation (DVC) algorithms were performed on the preprocessed μCT images of the 00 (reference) scan and 01 (deformed) scan to calculate the 3D kinematic field (displacement and strain field) before fracture. The 3D segmented microstructure and 3D kinematic field were integrated to analyze the local failure mechanisms of tensile SHCC specimens.

3.1. Preprocessing and visualization

Image preprocessing involves: a) transforming the slice images from 32-bit to 8-bit, b) removing the overlapped images between image stacks (an overlap of 20 voxels was set during the tile mode scans) [43], c) volume registration to preserve the same coordinate of 6 tomograms, d) Extracting the sub-volumes of 2240 × 2240 × 1200 voxels from the rotation center of the SHCC specimens to avoid edge effects and unnecessary background, e) eliminating noise and ring artifacts from the images through the 3D bilateral filtering [44] and 3D median filter with a small radius of 1 voxel, f) improving the contrast with a saturated pixel of 0.35, and e) slicing the 3D tomogram from left to right. All the above procedures were performed using Fiji open-source image processing [45]. After preprocessing, six 8-bit tiff tomograms were ready for analysis.

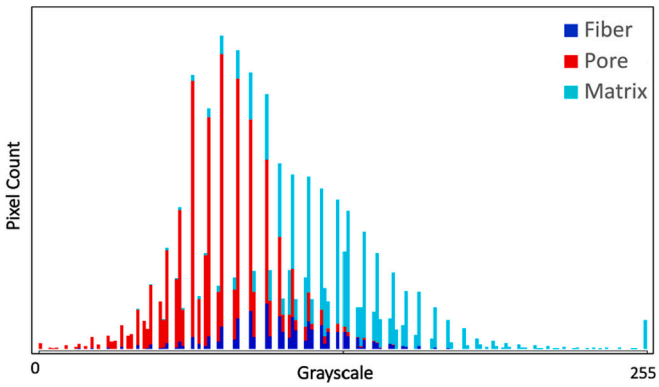

Fig. 4. Grayscale histogram of annotated voxels corresponding to fiber, pore, and matrix.

For 3D rendering and visualization, Tomviz (an open-source application for visualization of tomographic data) [46] was used to visualize the reconstructed 3D μCT images, segmented 3D μCT images of different phases, and 3D kinematic field from DVC. Dragonfly® analysis and visualization software (Object Research Systems (ORS) Inc.) was used to visualize the 3D fiber orientation and connectivity of pore networks [23,47].

3.2. Machine learning-based segmentation

Pixel-based image segmentation is one of the most crucial steps for the quantitative analysis of μCT. Traditional segmentation methods utilize only a few features (i.e., grayscale), which limit the accuracy and generalization capacity of the methods. As shown in Fig. 4, it is hard to distinguish and classify the pixels from fibers and pores based only on their grayscale.

In comparison, machine learning (ML) based 2D tomography segmentation methods (supervised learning classifiers) have been shown to be more robust, and have the advantage of automation and include multi-features [48–50]. In this study, six supervised ML models were built, trained, and evaluated based on the training and validation dataset. The ML model that achieved the best performance (segmentation accuracy and efficiency) was used to segment the whole preprocessed tomograms.

3.2.1. Dataset preparation

As the first step, manual annotations were conducted on every 200 slices to build the training and validation dataset to increase the variance and representativeness of the dataset because the adjacent slices are likely to be more similar to each other. For each selected 2D image, different regions (the most obvious objects corresponding to the target phases) were annotated as the corresponding phases (classes). In the manual annotations, three phases (classes) were separated from each other in images of SHCC specimens: fiber, matrix, and pore. Note that the pore phase contained voxels corresponding to voids, cracks, and background during the annotation and training of ML models. Since the image analysis was conducted on the entire SHCC specimen, the images must include the background voxels during the segmentation due to the specimen's external curvature and circular cross-section. The background voxels were separated from the void and crack voxels before the quantification analysis of the pore network. The manual annotation was performed with Fiji [45]. After annotations, 820,377 voxels were labeled, including 89,538 fiber voxels, 411,449 pore voxels, and 319,390 matrix voxels.

For feature engineering, grayscale, mean, median, minimum,

Table 4
Evaluation of ML models. (The scores here are weighted average scores of Fiber, Pore, and Matrix phases based on the validation set).

Model	Precision	Sensitivity	F1	MCC	ROC area	Training time (s)
Naive Bayes	0.890	0.816	0.840	0.772	0.960	30
Bayes Net	0.909	0.872	0.885	0.832	0.975	683
ANN – multiplayer perceptron (MLP)	0.977	0.977	0.977	0.993	0.965	33,930
Random decision tree	0.954	0.954	0.954	0.929	0.965	42
Logistic model tree	0.938	0.939	0.938	0.903	0.987	3,188
Random forest	0.980	0.981	0.980	0.970	0.999	303

maximum, Gaussian blur, Hessian, Sobel filter, membrane projections, bilateral filter, anisotropic diffusion, and difference of Gaussians were selected as the image features for the training of ML classifiers considering both segmentation accuracy and computing time [51]. Multiple 2D filters/convolutions with the default parameter combinations corresponding to the selected feature were applied to the training images for each selected feature. For instance, in feature engineering, multiple individual filters/convolutions of Gaussian kernels with the default sigma parameters were performed as the Gaussian blur features. The full dimensionality of the input feature vector is 170 (listed in Table S1, SI), which was the same for each image and model.

3.2.2. Model building and training

Six representative ML models were selected to classify the specimens: Naive Bayes [52–54], BayesNet [55–57], multiplayer perceptron (MLP) [58,59], decision tree [60,61], logistic model tree (LMT) [62,63], and random forest [64,65], which were trained using the manual annotations described in the previous section. Detailed information about each model was listed in the Table S2, SI.

Categorical cross-entropy loss between annotation and segmentation results was used as a loss function for model training. The stratified 10-fold cross-validation was used during the training to reduce overfitting and fit the imbalanced datasets. A two-stage strategy was also used for hyperparameter tuning, comprising of (i) Building the basic structure; and (ii) Optimizing parameter settings. During the optimizing stage, a manual grid search was utilized for hyperparameter tunning of all six models. Final hyperparameters for each model were also listed in the Table S2, SI.

3.2.3. Model evaluation

After training, the performance of each ML model was evaluated by comparing the annotation and predicted segmentation results of the validation data. F_1 score (Dice similarity coefficient), Matthews correlation coefficient (MCC), and receiver operating characteristic (ROC) area were calculated for each model because the dataset is unbalanced [66]. The F_1 score is the harmonic average of the precision and sensitivity (recall), with a maximum score of 1 indicating perfect precision and sensitivity and 0 as the worst [67]. MCC is used as a balanced measure of the quality of classifications even if the classes are of different size [68], which reflects the correlation between the prediction and ground truth. A maximum score of 1 indicates perfect matching between the segmented voxels and its ground-truth [69]. The ROC area, also known as AUC (area under the ROC curve), is also used to evaluate the segmentation method [70]. In addition, Precision, Sensitivity (Recall), and time taken to build the model are used to evaluate the segmentation models. The above evaluation metrics are defined as:

$$\text{Precision} = \frac{TP}{TP + FP} \tag{3.1}$$

$$\text{Sensitivity} = \frac{TP}{TP + FN} \tag{3.2}$$

$$\text{F}_1 = \frac{2 \times Precision \times Recall}{Precision + Recall} \tag{3.3}$$

$$\text{MCC} = \frac{TP \times TN - FP \times FN}{\sqrt{(TP + FP)(TP + FN)(TN + FP)(TN + FN)}} \tag{3.4}$$

where TP, TN, FP, and FN are defined per labeled voxel to represent the number of true positive, true negative, false positive, and false negative detections, respectively. A confusion matrix is used to derive all these parameters.

Notice that feature engineering, model training, and evaluation were performed with the Trainable Weka Segmentation plugin in Fiji and Weka® machine learning libraries [45,50,71]. The tests for calculation time were performed on Windows 10 Pro 64-bit Operating System, with one six-core Intel Xeon processor, CPU (E5-2643, 3.40 GHz), and installed memory (RAM) of 256 GB.

As a measure of segmentation performance, annotated voxels in the validation dataset are correctly segmented and calculated the corresponding precision, recall, F_1, MCC, and ROC. Meanwhile, lesser time taken to build the ML model represents greater efficiency.

The performances of different ML segmentation models are quantitatively shown in Table 4. The random forest model and the MLP model achieved the best performance related to segmentation accuracy, with the weighted average scores of F1 exceeding 0.97, MCC exceeding 0.97, and ROC exceeding 0.96. Compared with the random forest model, the time taken to build the MLP model was orders of magnitude larger due to the massive number of parameters needed in an artificial neural network (ANN). Although the Weka training platform only provided training time under the local CPU settings, the average classification time spend for each image was 37.5 s for the selected random forest model based on the segmentation of one tomogram. Considering the calculation efficiency, a random forest model was selected to segment the whole preprocessed in-situ tomograms.

Typical 2D segmentation results containing each of the three respective phases are given in Fig. 5, and the confusion matrix that highlights the accuracy in pixel classification results from the random forest model is shown in Table 5. The fine-tuned random forest model was utilized to segment the rest of the in-situ 3D images because high accuracies were achieved in the segmentations of different phases. The only small drawback is the sensitivity (89%) of the fiber phase, where around 5% of fiber pixels were predicted as pore pixels, and another 5% of fiber pixels were expected as matrix pixels.

3.3. Morphological and statistical analysis

3D morphological information of fiber objects and pore networks is essential to understand how the microfiber bridging helps form SHCC tensile ductility and crack width control and how the microfibers play a role during the SHCC loading and deformation processes. 3D morphological and statistical analyses were conducted on segmented fiber and pore phase images (binary images). More accurately, spatial distributions of fiber and pore, area distributions of fiber and pore along the Z-axis (height), fiber orientation (Phi and Theta angle), and pore connectivity were characterized based on 3D segmented images of the fiber and pore phases.

The spatial distribution of a specific phase (class) was characterized by three 2D density maps. A 3D segmented tomogram of the corresponding phase was projected into three orthographic 2D planes (OXY,

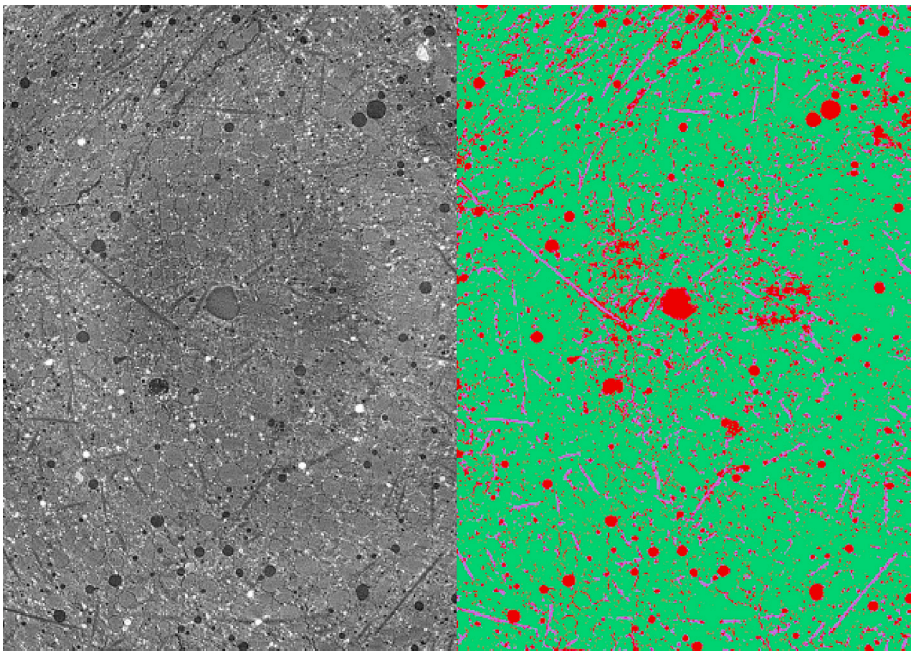

Fig. 5. (a) Reconstructed 2D μCT image; (b) Segmented image (green phase: matrix, red phase: pore, purple phase: fiber) of the random forest model. (For interpretation of the references to color in this figure legend, the reader is referred to the web version of this article.)

Table 5
Confusion matrix for the random forest model.

Phase		Predicted label		
		Fiber	Pore	Matrix
Actual label	Fiber	89.21%	5.28%	5.50%
	Pore	0.41%	99.07%	0.52%
	Matrix	0.40%	0.38%	99.22%

OYZ, and OXZ). The density value at each plane pixel is defined as the number of voxels segmented as the corresponding phase divided by the total number of voxels along the projection line. For the area distribution along the height, the cross-section areas of a specific phase along the height (Z-axis) were calculated from 3D binary images of the corresponding phase.

The fiber orientation and pore connectivity calculations are based on individual fiber and pore objects. As the first step, voxel connectivity analysis was performed based on a 6-connected voxel criterion, which means that the voxels are connected to form the "cluster/object" when the voxels share a familiar face. Note that the pore objects are usually made of at least two voxels, while fiber objects should be composed of at least 100 voxels (the diameter of PVA fiber is around ten voxel size). Therefore, the calculated objects (clusters) were refined by removing the connected components whose voxel count is smaller than the minimum value. Then, the refined objects were used to characterize the fiber orientation and pore connectivity.

To describe the morphology of fiber objects in 3D, each fiber's orientation (Phi and Theta angle) is defined as the orientation of the longest axis, which corresponds to the shortest eigenvalue of the inertia tensor of the 3D fiber object. As shown in Fig. 6, the value of Phi is the angle from the X axis of the projection on the XZ plane of the orientation, while the value of Theta is the angle from the X axis of the projection on the XY plane of the orientation.

Pore connectivity (expressed in %) is defined as the number of void voxels in the largest percolating pore object (cluster) divided by the total number of voxels attributed to pores in the volume of interest (VOI) [72,73]; it is a fraction of porosity, and equal to 100% when all the pores in the system are percolating. The calculations of 3D fiber orientation and pore connectivity were performed in Dragonfly®.

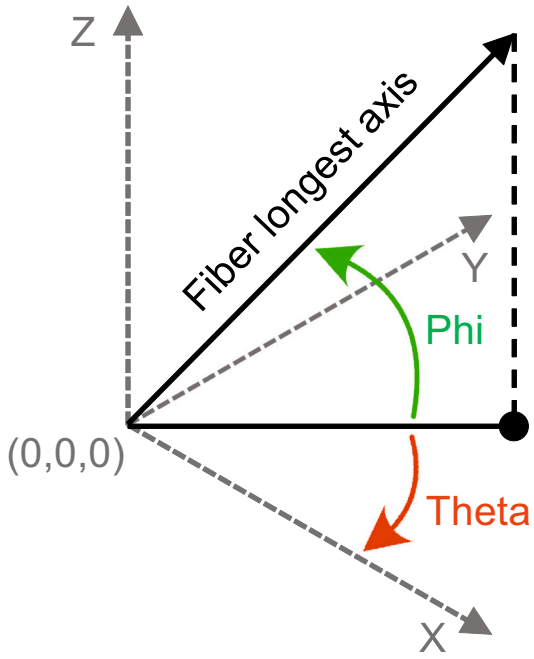

Fig. 6. Schematic representation of fiber orientation (Phi and Theta).

3.4. Digital volume correlation

Digital volume correlation (DVC) [74] is a powerful image processing method to measure the 3D kinematical fields (displacement and strain field) from the time series μCT images, especially the in-situ data set. DVC techniques calculate the displacement field by minimizing the correlation residuals (i.e., the sum of squared grayscale differences between the reference volume and the deformed volume corrected by the calculated displacement field [75]) under the hypothesis of conservation of the grayscale of the analyzed microstructure of images. Then, the

strain fields can be calculated from the displacement fields, and the 3D strain localization and local failure processes can be visualized and quantified [74,76].

In this study, the preprocessed μCT tomogram (2240 × 2240 × 1200 voxels^3) of 00 (reference) scan and 01 (deformed) scan was cropped to a VOI (the cubic subvolume) of 1300 × 1300 × 1200 voxels^3. The new VOI consists only of a cubic core of the SHCC specimen, which reduces the uncertainty and error inherent in the correlation residual caused by the uncertainty of the background's grayscale [77]. The regularized C8 element DVC algorithms (C8R) developed on Matlab by Bouterf [78,79] were selected to conduct the DVC analysis for tensile SHCC tomograms. The displacement fields were measured when discretized over a finite element mesh made of 8-noded cubes (C8) [80]. Since the strains before fracture were minor, a regularized approach was used [81,82]. For the mesh generation, the element size, which is comparable to the zone of interest (ZOI) size in classical Digital Image Correlation codes, was optimized to be 20 × 20 × 20 voxels^3 to reduce the computational complexity and uncertainty while still being able to capture complex displacement field and strain localization [81,82]. The regularized lengths were set to equal the element size so that the high-frequency displacement fluctuations, which are not mechanically admissible, are filtered out.

4. Fiber behavior associated micromechanics-based analysis for mechanical properties of SHCC

The micromechanics-based analytic modeling allows for systematic and practical tailoring of SHCC for high ductility and tensile strain hardening behavior by controlling the mechanical features of the composite matrix, the fiber, and the fiber/matrix interface. By deliberately allowing cracks to grow from pre-existing flaws, SHCC/ECC exhibits a high tensile ductility above 3%, 300 times that of regular concrete [83,84]. The typical cracking pattern under uniaxial tension results in many closely spaced microcracks of widths less than 100 μm [85,86]. The ductility of SHCC is the total sum of the distributed deformations resulting from these diffuse microcracks. To attain the multiple cracking responses in this controlled manner, SHCC must meet both strength and energy criteria. Brief explanations of strength and energy criteria are provided in Sections 4.1 and 4.2, respectively. The idealization of strength and energy criteria provides a systematic design approach for SHCC with desired tensile ductility, compressive strength, and workability. Detailed information on these criteria can be found in Li 2019 [14].

4.1. Strength criterion

The strength criterion states that the cracking strength (σ_c) required to initiate a crack from a pre-existing flaw must be less than the bridging capacity (σ_0) of the fibers crossing that crack (Eq. (4.1)). The satisfaction of the strength criterion ensures that there will not be a localized fracture on this crack plane. Crack initiation starts at the largest flaw most favorably oriented for fracture. Subsequently, the cracking progressively works to the next largest flaws as the tensile load increases. With the rise of tensile stress, more microcracks are gradually initiated.

$$\sigma_c < Min\left\{\sigma_0\left(already\ formed\ multiple\ cracks\right)\right\} \tag{4.1}$$

Once a microcrack forms, the load is transferred by the bridging fibers existing on the crack plane. The load carried by the bridging fibers is characterized by a σ(δ) relationship. The fiber bridging capacity peak value is different from one crack plane to another due to the non-uniform fiber distribution. If the strength criterion is violated on any existing crack plane, the crack results in a localized fracture, and multiple cracking processes are terminated. A "crack" with a cracking strength larger than the lowest bridging capacity of the existing crack plane will never be activated.

4.2. Energy criterion

The energy criterion is based on steady-state flat cracking (perpendicular to the applied load) so that SHCC can achieve multiple locations of simultaneously active cracking. To ensure this crack propagation mode, the crack tip toughness J_{tip} must be less than the complementary energy J_b'. The complementary energy can be calculated according to the σ(δ) relation as shown in Eq. (4.2). The crack tip toughness is the energy equivalent of the matrix fracture toughness and is defined in Eq. (4.3).

$$J_{tip} \le \sigma_0\delta_0 - \int_0^{\delta_0} \sigma(\delta)d\delta \equiv J_b' \tag{4.2}$$

$$J_{tip} = \frac{K_m^2}{E_m} \tag{4.3}$$

where σ_0 is the bridging capacity of the fibers corresponding to the critical crack opening δ_0; K_m is the matrix fracture toughness; and E_m is Young's modulus of the matrix. Eq. (4.2) employs the concepts of energy balance among external work ($\sigma_0\delta_0$), energy absorption through fiber/matrix interface debonding and sliding (the integration term), and crack tip energy absorption through matrix damage (J_{tip}). This energy criterion determines whether the crack propagation mode is steady-state flat cracking or Griffith cracking.

4.3. Improvement on information about fiber orientation and crack opening

Based on the strength and energy criteria, a micromechanics-based model has been developed to design an engineered cementitious composite (Li 2019 [14]). The fiber orientation has been assumed in random 2D or 3D uniform distribution. However, as mentioned in Section 4.1, the peak value in the strength criterion, the fiber bridging capacity is different from one crack plane to another due to the non-uniform fiber distribution. Therefore, this assumption could result in an under- or over-estimation of the cracking strength due to the lack of direct observation of fiber orientation in these strain-hardening cementitious composites. As mentioned in Section 4.2, theoretically, the observed crack opening should be smaller than the critical crack opening δ_0. However, the actual crack opening is difficult to know without direct observation. Although specific methods (e.g., measurement of residual crack opening after unloading [87] or digital image correlation [88]) have been used, it is difficult to identify the crack opening under loading conditions.

The goal is that the challenges mentioned above can be addressed using the ML-based in-situ microtomography segmentation method developed in this study. The fiber orientation and cracking opening are measured considering the method described in Section 3. With the new method, the assumed fiber orientation in the model can be replaced by direct and more accurate measurements of in-situ fiber orientation; the strength, such as peak value, could be more accurately estimated. Since

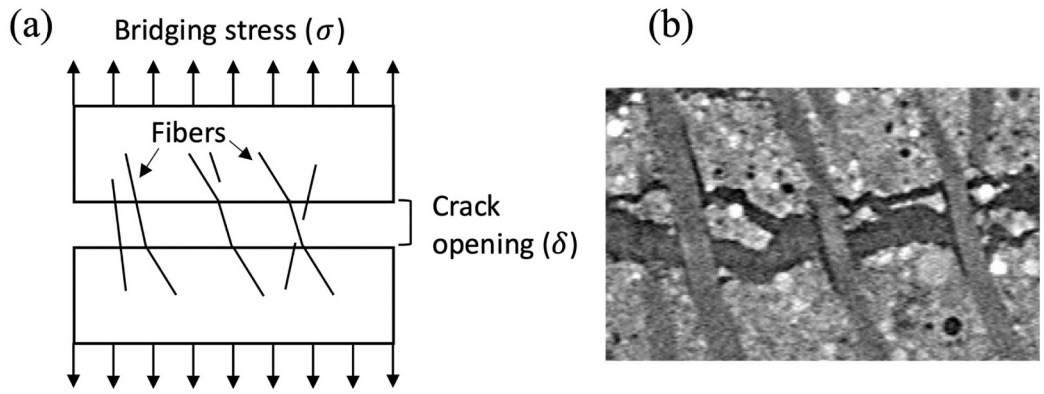

Fig. 7. (a) Schematic fiber behaviors in SHCC with different embedment length and inclination angles; (b) Experimental fiber behavior around the crack plan in SHCC at 02 scan from Fig. 9(c).

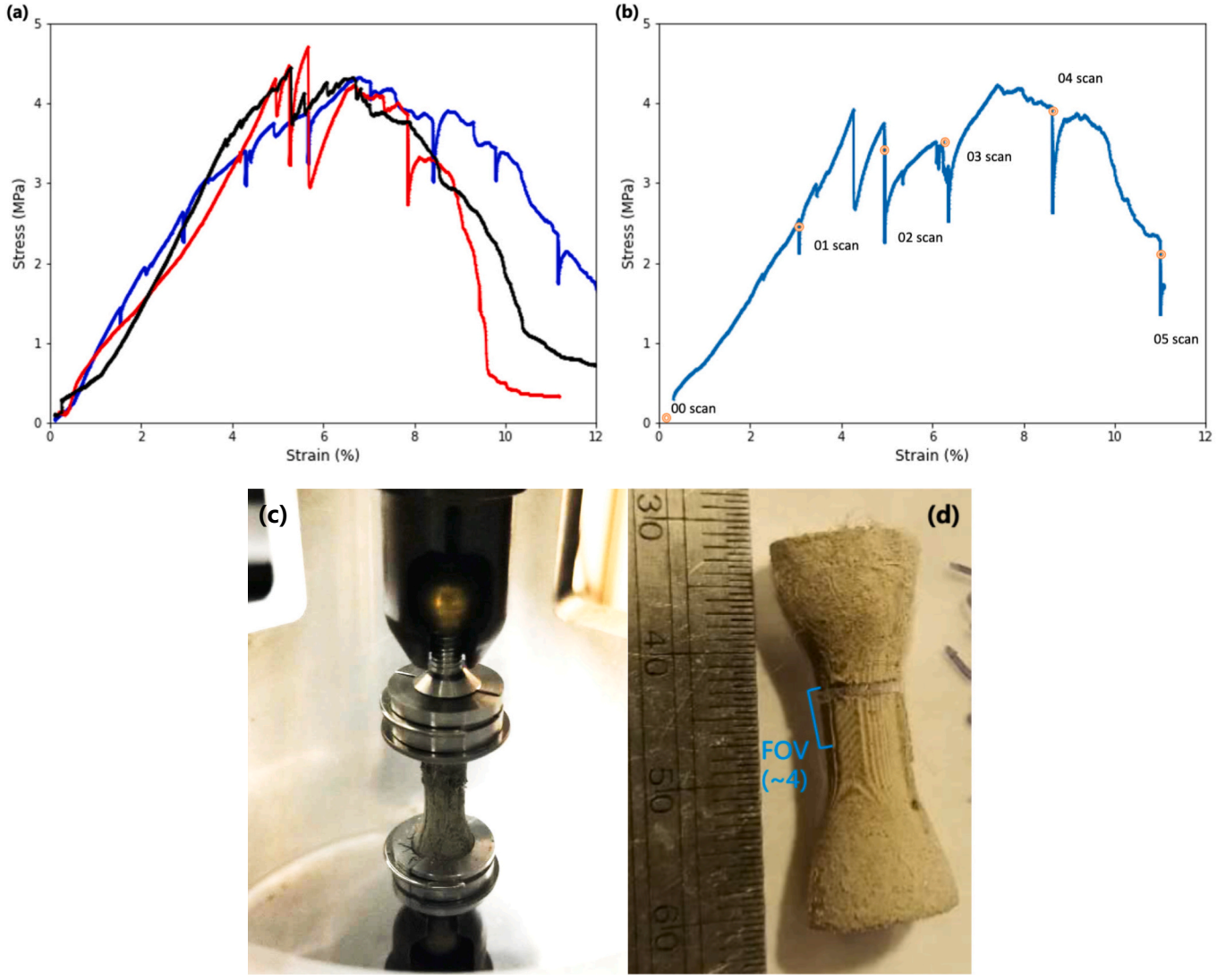

Fig. 8. Uniaxial tensile test data and sample: (a) the σ-ε relationships of preliminary tension tests, (b) the σ-ε relationship of the in-situ tension test, (c) the specimen during the in-situ tension test, and (d) the specimen after the in-situ tension test.

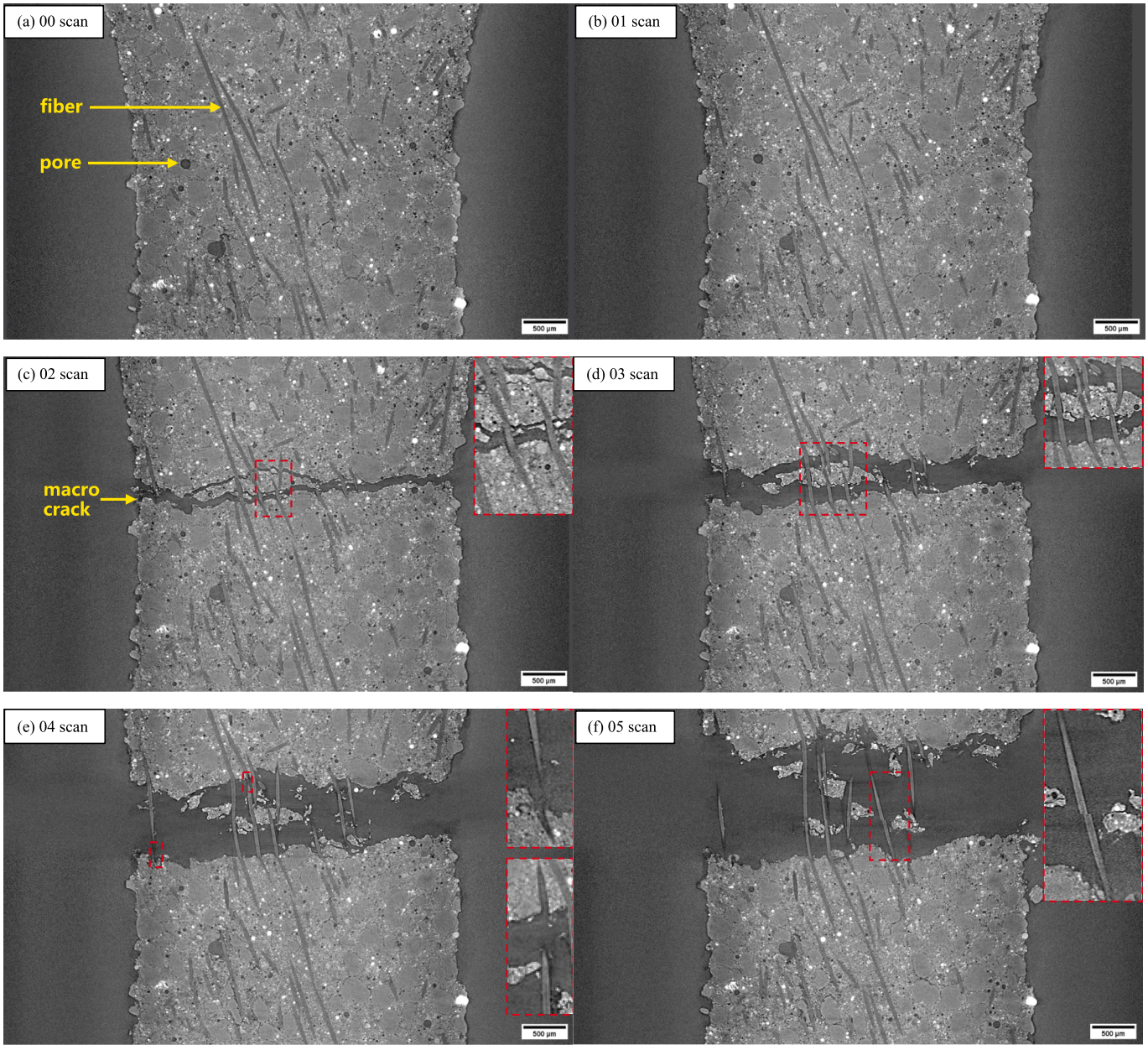

Fig. 9. Selected 2D μCT slices acquired during the in-situ uniaxial tensile test corresponding to the scans shown in Fig. 8b.

the fiber bridging, stress-crack opening (sigma-delta) behavior is an integration of the pull-out behavior of all individual fibers on the crack plane, which is not only affected by the fiber properties and fiber/matrix interactions but also the fiber content and fiber orientation. The improved information on fiber orientation can help enhance the prediction of the sigma-delta behavior of strain-hardening cementitious composites. The model used in this study is based on the previously developed model by Yang 2008 [15], where the information on fiber orientation has been improved with the introduction of direct measurements from the microtomography segmentation method. The direct observation of crack opening could also be used to correlate the in-situ crack opening under the loading condition. Expanding upon prior work, Section 5.4 presented and discussed the preliminary results of the stress-crack opening behaviors predicted by both the reference and improved models. The reference model was based on the uniform distribution assumption of fiber orientation. In contrast, this study observed the enhanced model integrated with the in-situ fiber orientation distribution.

Finally, the direct observation of the fiber behaviors in SHCC could be used to verify the previously proposed illustration of randomly oriented fibers relative to a crack plane (Fig. 7), where the fibers could undergo debonding, sliding, complete pull-out, or fracture at a given crack opening.

5. Results and discussion

5.1. Direct observation

Before the in-situ tests with μCT, preliminary mechanical tests were performed to assess the mechanical response of the SHCC specimen and estimate the load/displacement at which the displacement should be held for μCT scanning for the subsequent in-situ experiments. As shown in Fig. 8a, the SHCC specimens tested at 28 days displayed an ultimate tensile strength of between 4 and 5 MPa with a high tensile strain capacity exceeding 7%. The stress-strain curve for in-situ uniaxial tensile test is shown in Fig. 8b, where both the ultimate tensile strength and the

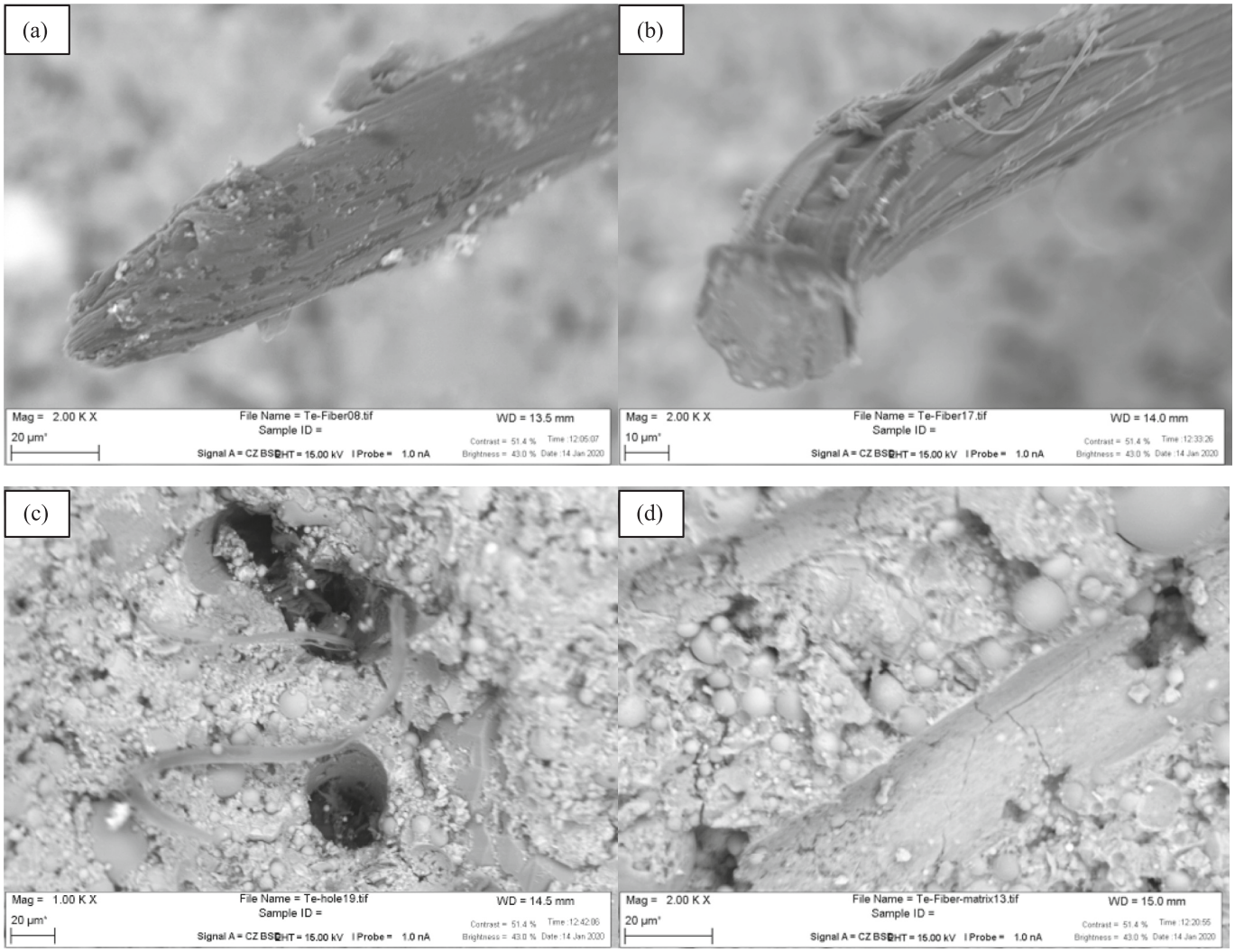

Fig. 10. SEM images of a fractured cross-section of SHCC specimen after tensile test. Enlarged PVA fiber tips subjected to (a) fiber fracture corresponding to Fig. 9f, and (b) fiber pullout corresponding to Fig. 9e. (Magnification at 2000 under Secondary Electron Mode); PVA fiber/matrix interface in the views of (c) holes with protruding PVA fibers, and (d) matrix.

strain capacity were very similar to the values in the preliminary tests. The mechanical displacement caused the high strain during earliest portion of the small-scale in-situ uniaxial tensile test, and the data have been adjusted to account for this initial nonlinear response caused by slippage of testing components.

During the loading process, six µCT scans were made. The 00 scan was conducted at the initial state, while the 01 scan was made once the first stress drop was observed. Note that the stress drop at 01 scan could result from either specimen stress relaxation in tension or micro-crack propagation outside the FOV. The 02 scan was made once the first crack was observed in the FOV. From scan 03 to scan 04, each scan was conducted in sequence during the evolution of the crack network. Finally, the 05 scan was made when the specimen was fractured in the uniaxial tensile test. The large stress relaxations during the µCT scans were inevitable because each high-resolution µCT scan took around 45 min and a constant controlled displacement was held during these periods.

5.2. Qualitative analysis of reconstructed 2D µCT slices and corresponding SEM images

The time series 2D slices (Fig. 9) of the same location from the corresponding µCT scans provide qualitative observations of major crack formation and fiber behavior during the uniaxial tensile loading. Just after the formation of the first cracking network in the FOV, the crack widths ranged from 30 µm to 150 µm, as shown in Fig. 9c. Meanwhile, fiber deformation (as bending) developed around the cracks. Note that the crack network had already propagated through the cross-section, and fiber bridging is the primary toughening mechanism after the 02 scan. The crack width grew when the displacement increased from 02 scan to 03 scan. The bend angle of fibers raised, the bend radius of fibers decreased, and the inclined angle between fiber and matrix increased. From one side, snubbing at the fiber exit point increases the friction against fiber pull-out, effectively raising the fiber bridging force. On the other side, the above morphological changes represent damages to the bent fibers, including micro-cracks (Figs. 9c and 10), and reduce their strength, which effectively lower the fiber bridging force [89,90]. Therefore, as the displacement further increased, fiber pullout was observed around 04, and a fiber shear fracture was observed in the 05 scan. Scans 02–05 also revealed matrix damage by a relatively large spall involving a group of crack bridging fibers. As the crack opening increased, the large spall broke into smaller pieces. In summary, with increasing tensile loading, cracking propagation, fiber bending, fiber fractured, fiber pull-out, and progressive matrix damage were observed in sequence. This is the first time the complex evolving processes of crack bridging fibers were observed in detail during strain-hardening in

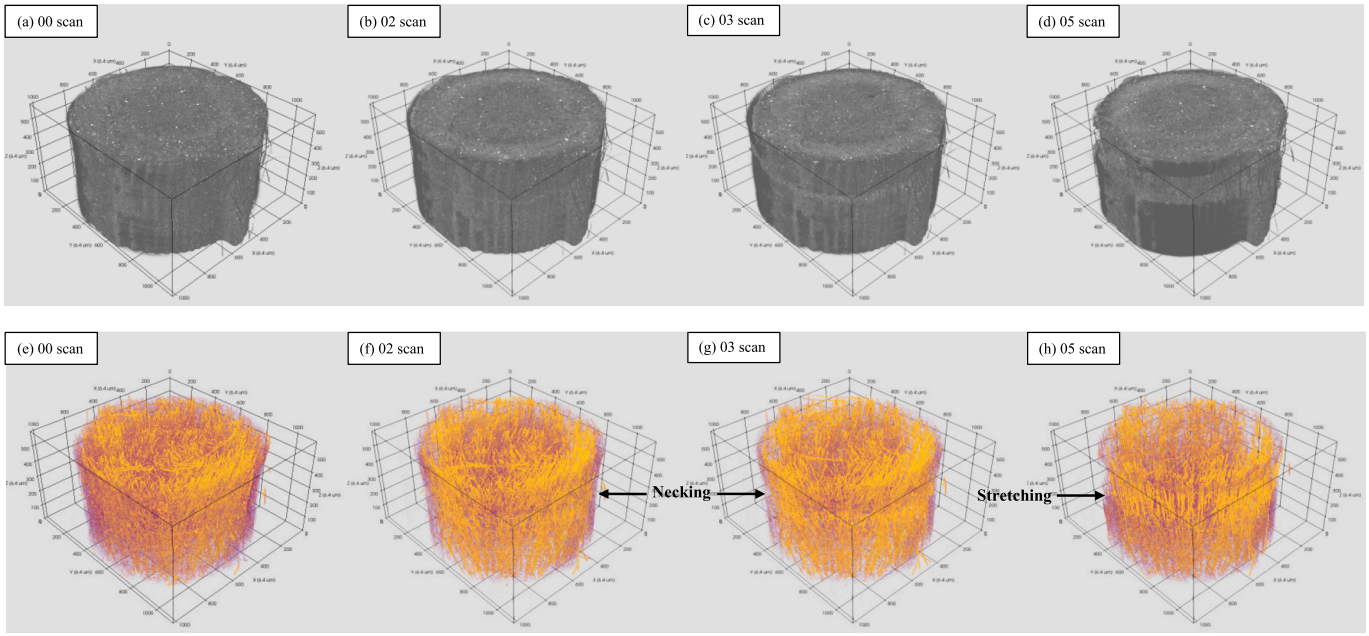

Fig. 11. The 3D rendering of reconstructed tomography (top) and segmented fiber phase (bottom) for ROI of the in-situ tested specimen corresponding to the scans shown in Fig. 8.

SHCC/ECC.

The observations of 2D μCT images coincide with the observation from the SEM results (Fig. 10) on the cross-section of a fractured SHCC specimen, and the higher resolution and magnification of the SEM images of the post-fractured sample provide further information on the damage mechanisms. Specifically, tapered fiber tips and adherent cementitious matrix at the tip, as revealed in Fig. 10a and b, indicate fiber fracture. The rest of the images suggested that PVA fibers are subjected to surface abrasion when pulled out from the cementitious matrix, providing a frictional bond at the fiber/matrix interface. PVA leftover due to the strong bonding was also observed in Fig. 10c and d. The existence of protruding fibers may reflect strong bonding and fracture fibers but may also be associated with the short, embedded length of the fiber pulled out during the crack opening process.

In summary, considering the 2D μCT and SEM images, it is observed that with increasing tensile loading, cracking propagation and branching, fiber bending, fiber surface damage and fracture, and fiber pull-out were observed in sequence. Changes in the fiber morphology play an essential role in the toughness mechanism in SHCC.

5.3. ML-based μCT segmentation results

The 3D rendering of selected preprocessed tomograms and segmented fiber phase from the selected μCT scans are presented in Fig. 11. The response is typical of an SHCC specimen under uniaxially tension loading. At the beginning of the loading (before the 02 scan), the SHCC matrix resisted most of the tensile force. After introducing cracks, the tensile force at the cracking cross section was resisted by the fibers that bridged the top and bottom surfaces. Therefore, the fibers around the cracking were stretched vertically (along the Z-axis) around the crack network. Just before failure (05 scan), nearly all the fibers in the elongate crack opening zone were distributed vertically. In the following section, the quantitative and statistical analysis of the fiber morphology will explain the observations of fiber behavior and resistance mechanism in the in-situ μCT images (Figs. 9 and 11).

5.4. Fiber orientation and spatial distribution

To make an in-depth study on the fiber behavior during the uniaxial tensile test and provide data for micromechanics-based analytic modeling, the 3D orientation for each fiber object was calculated (Fig. 12). As stated in Section 3.3, the Phi angle is equal to the rotation of the X-Y plane towards the Z-axis and the Theta angle is equal to the rotation of the X-axis towards the Y-axis. For the necking region, an increase of strain was expected as more fibers are oriented vertically (around a 90-degree Phi angle, labeled by green color) with the evolution of the cracking network. This means fibers took an increasing percentage of uniaxial tensile loading in the necking region. For the fibers within the top and bottom uncracked SHCC matrix, there are no noticeable orientation changes for the Phi angle. In the top and bottom uncracked regions, multiple connected fibers were incorrectly labeled as blue (0-degree Phi angle) or red (180-degree Phi angle) because these connected fibers were incorrectly recognized as one fiber object due to the limitation of the 6-connected voxel criterion. The longest axis of these connected fiber objects is oriented horizontally (0/180-degree Phi angle). Improving the accuracy of voxel connectivity analysis with more advanced criteria is important, but it is beyond the scope of this paper.

For the Theta angle, it is hard to make a solid conclusion only based

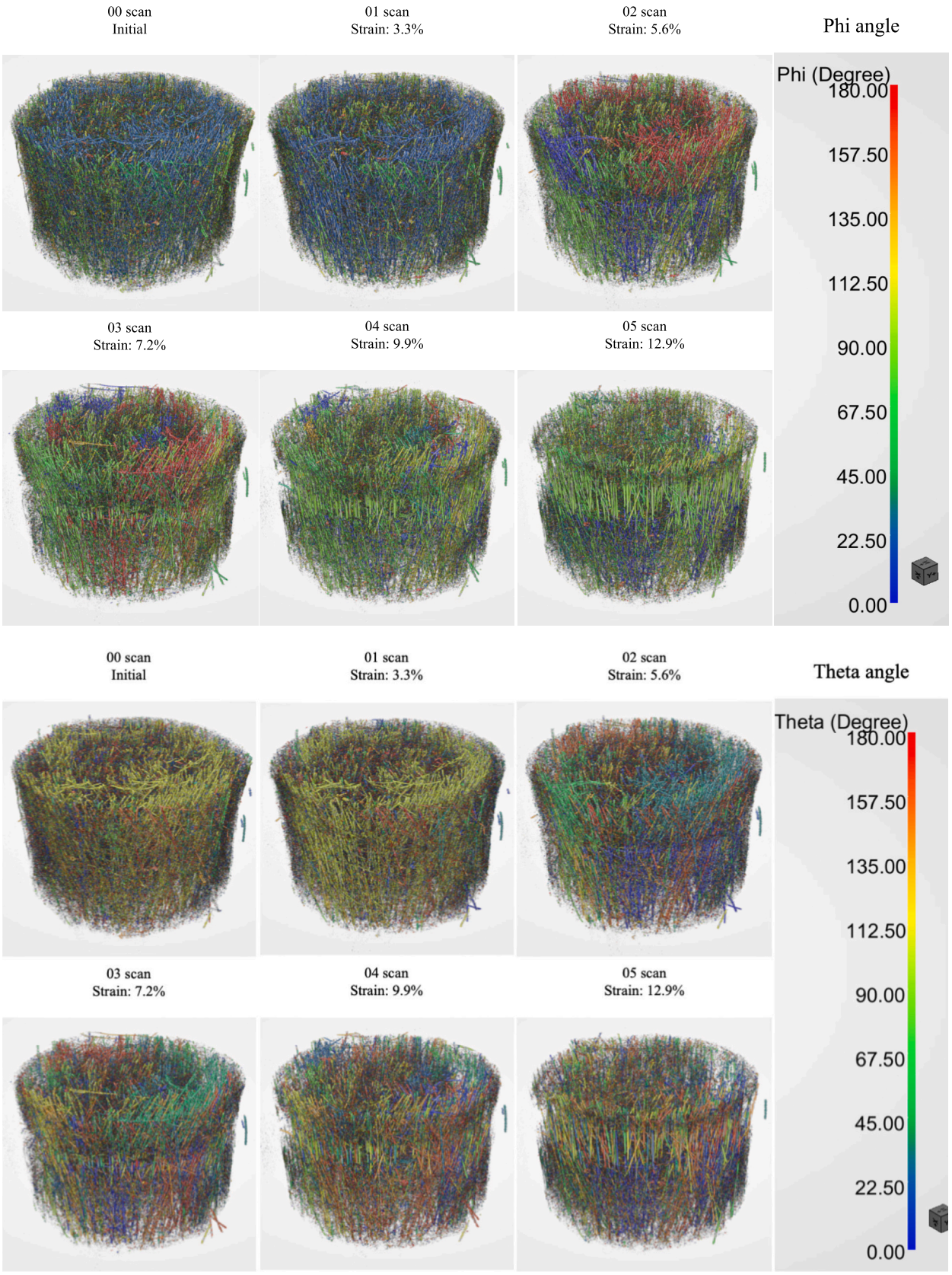

Fig. 12. The 3D rendering of fiber orientation for Phi angle (top) and Theta angle (bottom) for ROI of the in-situ tested specimen corresponding to the scans shown in Fig. 8.

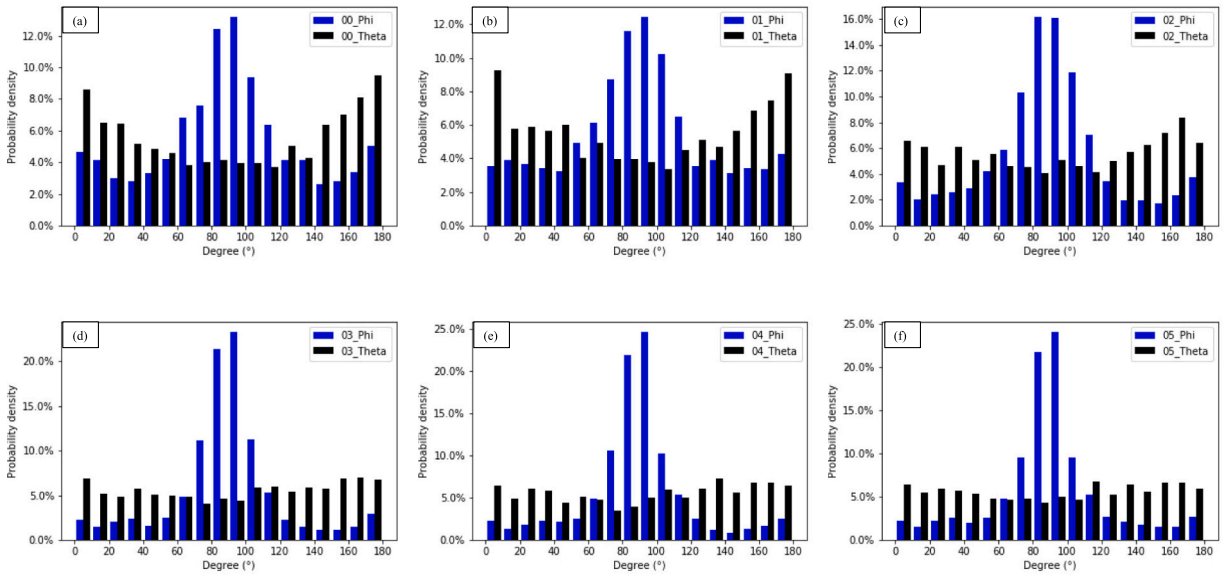

Fig. 13. Fiber orientation histogram for ROI of the in-situ tested specimen corresponding to the scans shown in Fig. 8.

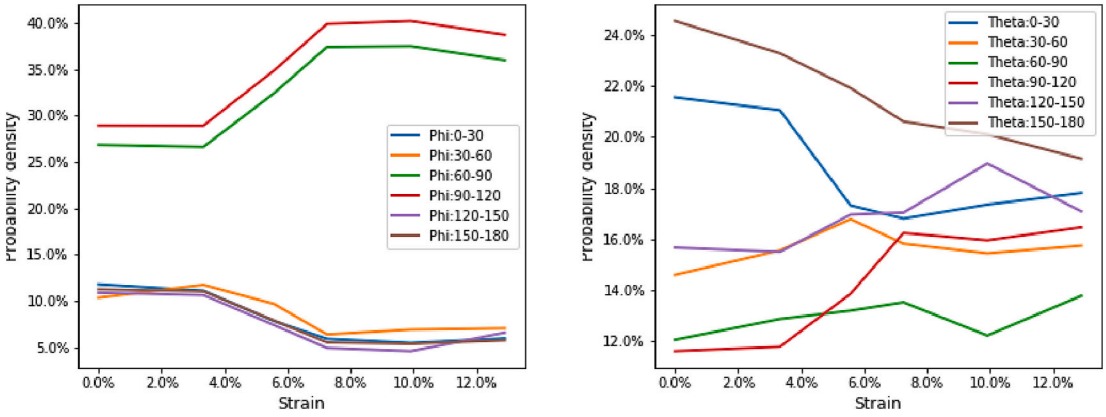

Fig. 14. Fiber orientations of (a) Phi angle and (b) Theta angle as a function of tensile strain.

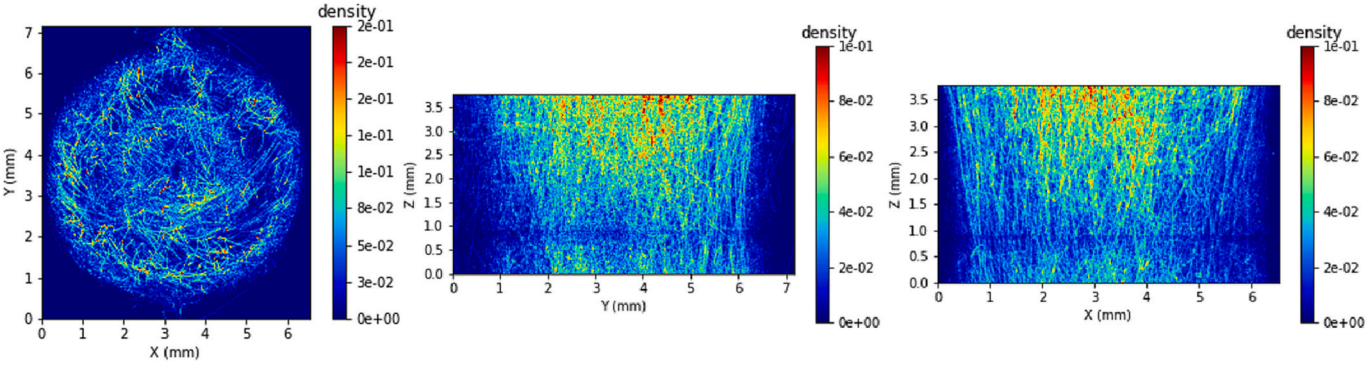

Fig. 15. Fiber spatial distribution for ROI of the in-situ tested specimen at initial state (scan 00).

Table 6
Comparing stress-crack opening results from the experiment, improved model in Section 4.3, and reference model based on statistics of fiber morphology.

	Experiment result		Improved model based on fiber's orientation from image analysis		Reference model based on uniform distribution of fiber's orientation	
Scan	Stress (MPa)	Crack opening (um)	Stress (MPa)	Crack opening (um)	Stress (MPa)	Crack opening (um)
02	3.75	143 ± 20	3.78	140	3.06	138
03	3.80	326 ± 37	3.82	150		

on visual observation. Therefore, further statistical analysis on the fiber orientation was conducted. To avoid the incorrect orientation angles of the connected fiber objects, the fiber objects with more than 5×10^5 voxels (considering the maximum volume of a single fiber) were ignored during the calculation of the fiber orientation distribution histogram from the results of Fig. 13.

The fiber orientation distribution histograms for each scan were calculated (Fig. 13), which are utilized in the fiber behavior analysis and the associated micromechanics-based analysis for the mechanical properties of SHCC. For the initial (00 scan) phi angle, the fibers show a predominant orientation of phi angle ranging from 70° to 110°, which is a result of the casting technique of the small specimens, as also described in other works [25,26]. For the time series distribution of phi angle, the percentage of phi angle ranging from 80° to 100° increased, the percentage of phi angle at 70° and 100° kept similar; and the others decreased. For theta angle, the percentage of theta angle below 30° and above 150° decreased, while others increased. The distribution of theta degree tended to be homogeneous. Besides, all the major changes mainly happened around the 02 step when the major crack network propagated.

Fig. 14 shows the relationship between fiber orientation and tensile strain. A crucial finding is that when the strain increases from 8% to 12% (from 04 scan to 05 scan), the volume fraction of vertically oriented fiber (phi angle ranging 60°–120°) decreases at high tensile strain and stress values. The above results indicate pull-out and fracture of the vertically stretched fibers between the 04 scan and 05 scan, which caused the reduction of the uniaxial tensile strength of the specimen to decrease (Fig. 8) and the failure of the testing specimen.

5.5. Mechanical properties based on micromechanics and image analysis

The fiber spatial distribution is also an important index for the quality of SHCC specimen and micromechanics-based analysis. As shown in Fig. 15, the 2D projected fiber density maps from three axes were calculated. The results show a homogeneous spatial distribution of fibers in three directions. In the following micromechanics-based analysis, a homogeneous distribution of fibers along the height of the specimen was assumed.

Table 6 compares stress-crack opening results among the in-situ experiment, the micromechanics-based predication improved by the measured orientation of fibers, and the original micromechanics-based prediction using the uniform distribution assumption for fiber's orientation. 02 scan and 03 scan were selected because the first crack in FOV was observed at the 02 scan, and the specimen almost failed after the 03 scan. For experimental result, the corresponding stress values were calculated from Fig. 8. The crack opening in the in-situ experiment was measured by mean and standard deviation at four distributed locations along the crack plane in Fig. 9. For reference model prediction, an assumption of uniform distribution for fiber's orientation was applied [14]. For improved model prediction, the calculated stress and predicted crack opening were calculated using micromechanics-base modeling, as stated in Section 4.

As shown in Table 6, the improved model integrated with the in-situ fiber orientation provided dynamic prediction results and accurately predicted stress-crack opening at the 02 scan when the first crack in FOV was observed. Compared to the experimental results, the stress values are the same. The calculated crack opening of the improved model was within one standard deviation from the mean value of the actual (experimental) crack opening. In comparison, the reference model only provided a static prediction for the stress-crack opening because of the uniform distribution assumption of the fiber's orientation. The predicted strength was lower than the experimental results, which implies that previous research underestimated the strength and provided a high safety factor for the structural design. For the calculated crack opening, no significant difference was observed between the improved model and reference model because the fiber's orientation coupled with other factors in calculating the crack opening. At the 03 scan, the computed crack opening of the improved model was below the range of three standard deviations from the actual crack opening because of the further expansion of the single crack opening within the FOV. The number of micro-crack openings in the testing specimen was limited (only three)

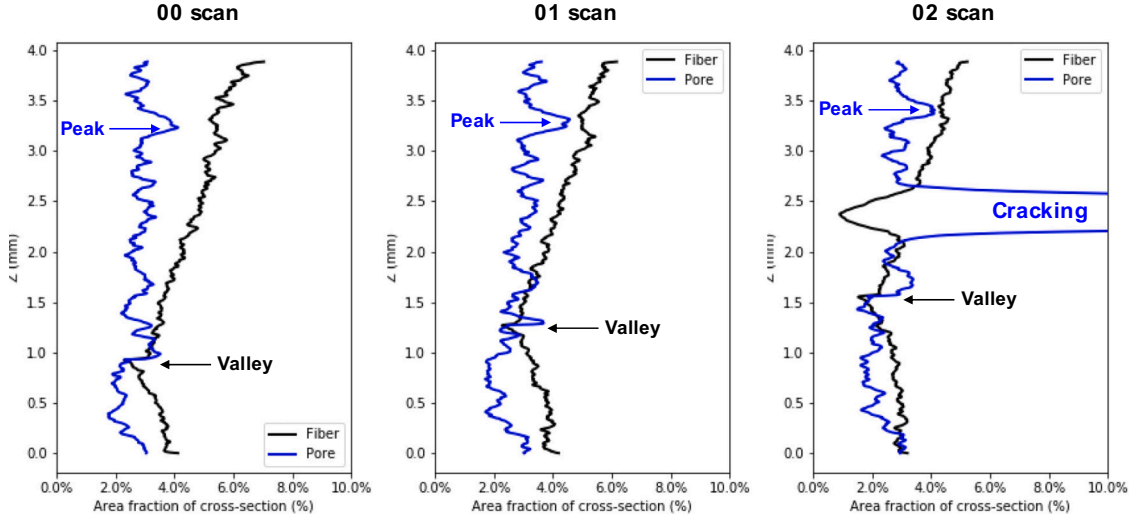

Fig. 16. Area distributions of fiber and pore along the specimen's Z-axis (the tensile loading direction). The area was normalized using the mid-height cross-section area of the specimen as the area fraction (The VOIs in Figs. 16 and 17 are the cubic subvolumes with a size of 1300 × 1300 × 1200 voxels^3 at the center of FOV in Fig. 11).

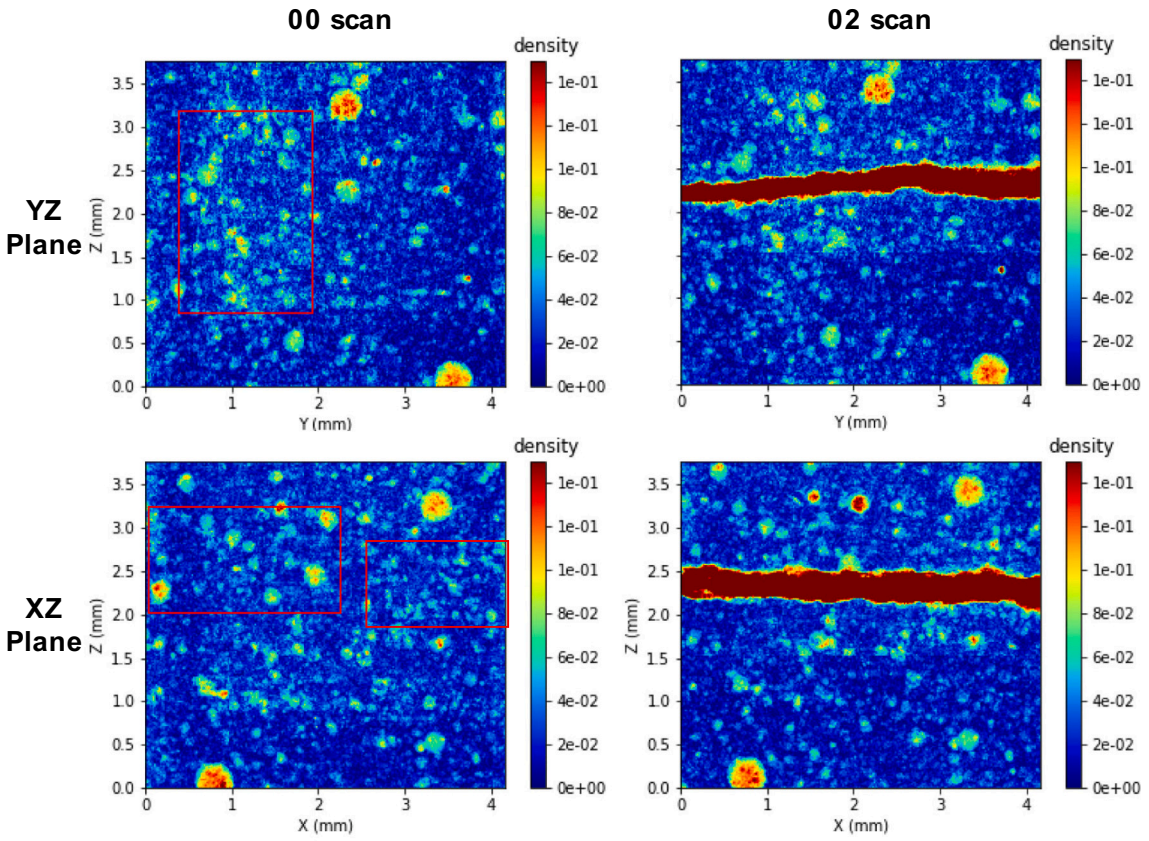

Fig. 17. The 2D projected pore density of segmented pore phase at 00 scan and 02 scan. The red rectangles highlight the 2D regions where the localizations of pores happened. The VOIs in Figs. 16 and 17 are the cubic subvolumes with a size of 1300 × 1300 × 1200 voxels^3 at the center of FOV in Fig. 11. (For interpretation of the references to color in this figure legend, the reader is referred to the web version of this article.)

due to the short gauge length (12 mm) of the specimen, which is beyond the hypothesis (e.g., steady-state flat cracking) for the micromechanics-based analytic modeling in Section 4. Therefore, the micromechanics-based model integrated with fiber orientation's distribution achieved accurate in-situ calculation results for the fiber bridging stress-crack opening (sigma-delta) behavior for the steady-state flat cracking. The model can be further improved by integrating the ratios of fibers that undergo debonding, sliding out, completely pulled out, or fractured at a given crack opening.

5.6. Failure mechanism analysis based on fiber distribution and microstructural properties

Fig. 16 presents the evolution of the area distributions along the tensile loading direction for both fiber and pore phases. At the initial state (00 scan), the largest pore area fraction (the blue peak) was observed at the height of around 3.2 mm, and the smallest fiber area fraction (the black valley) was observed at the height of about 0.9 mm. From the 00 scan to the 02 scan, the height of the blue peak increased by 0.3 mm while the height of the black valley increased by 0.6 mm at the same time. Thus, the tensile displacement fields of the pore phase and fiber phase in this SHCC specimen were different if the cross-section of the largest pore area fraction and the cross-section of the smallest fiber area fraction were utilized as the referenced planes. Moreover, as shown in the 02 scan of Fig. 16, instead of initiating and propagating at the height with the smallest fiber area fraction or largest pore area fraction, the major cracking propagated at the height between the peak of the pore area fraction and the valley of the fiber area fraction (at the height around 2–3 mm). Fig. 17 gathers the 2D maps for projected pore density of segmented pore phase at 00 scan and 02 scan. The major cracking in the 02-scan propagated through the regions where pore networks localized at the initial state (00 scan).

Fig. 18 shows the 3D renderings of pore connectivity from the initial state (00 scan) to the cracked state (02 scan) and strain field just before cracking (01 scan) to describe the complex pore structures and heterogeneous strain fields under uniaxial tension. Comparing Fig. 18 (a) and (b), almost no change in the pore microstructure has been observed between the initial specimen and the specimen before cracking. Only in some weak points/regions (large connective pores) of the testing specimen did the displacement incompatibilities under uniaxial tension led to stress concentrations, resulting in local strain localization before cracking. The presence of pores inside the microstructure causes stress concentrations in the areas surrounding the pores under vertical uniaxial tension. The strain localizations (Fig. 18(c)) are thus observed around the connected pores with volume exceeding 0.01 mm^3 (pore objects mapped as green, yellow, and red in Fig. 18(a)), even though no damage is visible in both the 2D μCT slices (Fig. 9) and segmented pore phase (Fig. 18(b)). When the load increased, the cracking network (Fig. 18(c)) propagated through the identified regions of localized strains. Thus, Fig. 18 indicates that the regions with strain localizations around the connected pore led to the development of the cracking network in the SHCC specimen under the uniaxial tensile experiment.

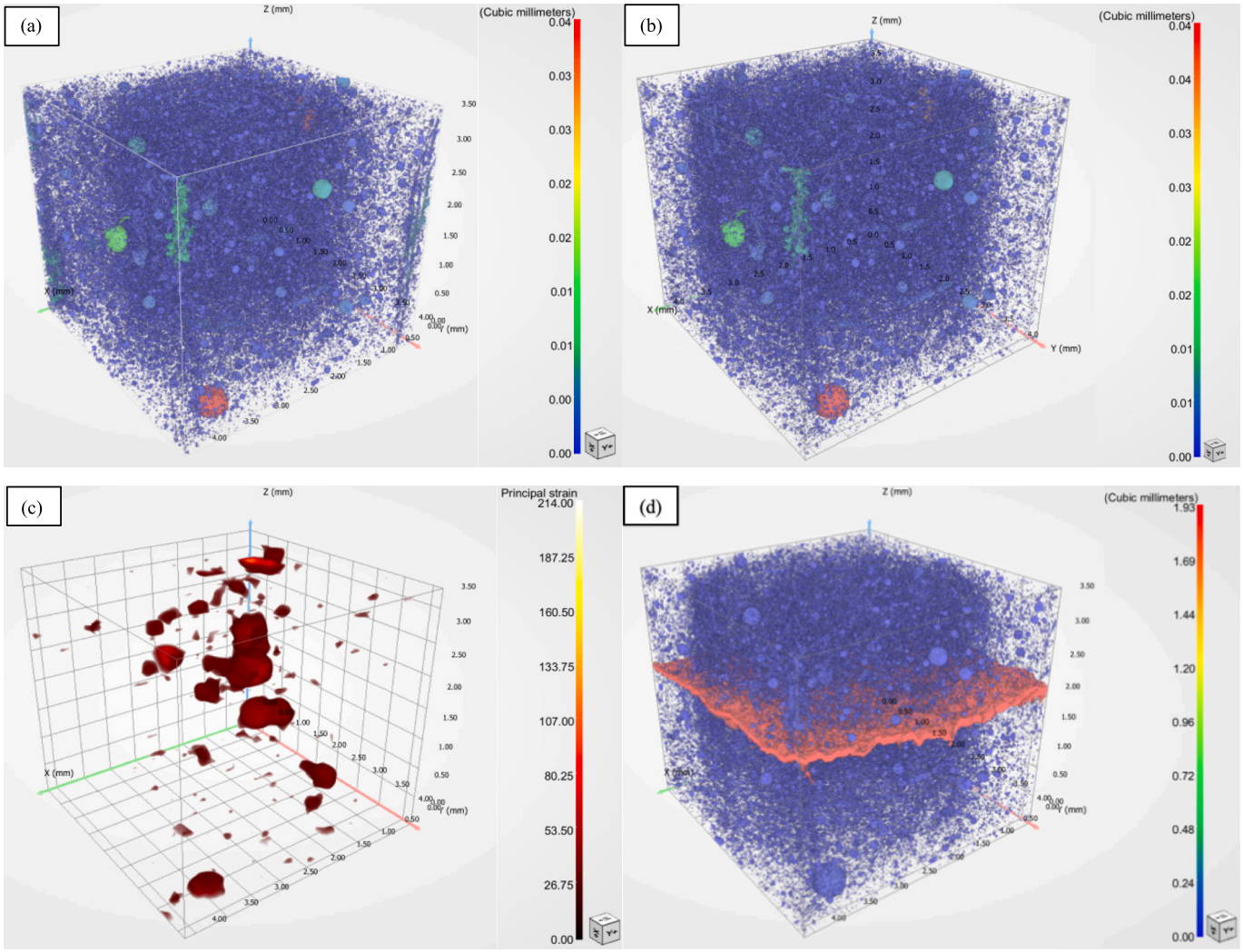

Fig. 18. The 3D rendering of (a) connected pore network in the order of increasing volume at 00 scan (initial state), (b) connected pore network in the order of increasing volume at 01 scan (before cracking), (c) major principal strain ε_{eq} field at 01 scan (before cracking), (d) connected objects for pore phase in the order of increasing volume at 02 scan (after cracking).

6. Conclusions and future directions

This research work investigated the microstructure evolutions of strain-hardening cementitious composites (SHCC) under the in-situ uniaxial tensile test. A state-of-the-art machine learning-derived pipeline for automated μCT image processing and analysis was developed to investigate SHCC's microstructure systematically. The random forest model achieved high performances in segmentation accuracy tasks and efficient calculation in processing the 3D tomograms. The in-situ evolution of segmented microstructures of SHCC during tensile loading, especially the strain-hardening process, was directly observed, quantified, and analyzed for the first time. In the in-situ microtomography segmentation analysis (MSA), the advanced algorithms and prototype software quantified the structure, distribution, orientation, and connectivity of the pores, cracks, and fibers in SHCC based on the μCT images. The quantified information and model were then used to develop more realistic micromechanics-based models for the fracture or durability of SHCC structures. At the same time, rigorous mathematical analysis of the strain and stress fields was performed using a digital volume correlation (DVC) method to provide a broader perspective about crack initiation and propagation from experimental mechanics.

The experimental results show that fibers reinforced the fracture planes in the SHCC through fiber debonding, bridging, bending, stretching, pulling out, and fracturing in the tension zones during the in-situ test. The in-situ fiber behavior and pore evolutions contributed to understanding ductility and toughness in SHCC. For pore phase analysis, the major cracking propagated through the regions where pore networks localized at the initial state during the tensile test. The regions with strain localizations around the connected pore led to the development of the cracking network. Based on the in-situ analysis of pore size distribution, filling the pores within a specific size range using micro-scale fine aggregate may further improve the cracking strength of the specimen. For fiber behavior analysis, a homogeneous spatial distribution of fibers can be observed in three directions. However, the orientation distributions showed inhomogeneity due to the layer-by-layer casting method. During the in-situ tests, fibers in the tensile zones were subjected to surface abrasion when pulled out from the cementitious matrix, which provides a frictional bond at the fiber/matrix interface. The changes in fiber orientations in the Phi and Theta angles contributed to the diffusion of multiple microcracks and crack width control. The micromechanics-based analytic modeling was improved by using the dynamic information of the fiber behavior (e.g., in-situ distribution of fiber orientation in this research) in SHCC. Statistical information on the fiber distribution and the fiber orientation extracted from the in-situ μCT reduced the variability of fiber behaviors in SHCC, especially when the composite undergoes cracking stages, and enhanced the predictability of

existing micromechanics-based models. Accurate calculation results for the fiber bridging stress-crack opening (sigma-delta) behavior when the first major crack was observed in SHCC. For local analysis on microscale ROI, the strain localization was observed around the connected pores with a volume exceeding 0.01 mm^3, and multi-cracks propagated through these regions during the uniaxial tensile test.

For future directions, this work built a machine learning-based microtomography image characterization pipeline for cementitious materials under load. Improvements can be made in the following fields:

- Improve the ML-based segmentation: the recently advanced DNN models (e.g., U-Net model [26,33,34], visual transformer (ViT) model) accelerated by the GPU and distributed computation have improved performance in both accuracy and efficiency significantly.
- Improve the accuracy of 3D kinematical fields (displacement and strain) by using the 3D segmented phase (e.g., aggregates) to calculate the kinematical fields [91].
- Introduce volumetric distribution and morphologies (e.g., length of each fiber) of segmented phases into the micromechanics-based modeling of cementitious materials with multiple phases (e.g., SHCC, steel reinforced concrete).
- Apply the same pipeline to characterize the multi-crack propagation in the ECC material.
- Apply the same pipeline to characterize the pore network (e.g., pore size distribution, pore connectivity) to understand the durability and transport properties of cementitious materials under environmental exposure.

In summary, in-situ synchrotron X-ray microtomography with loading provides the state-of-the-art characterization for the various micro-scale information of material and composition in concrete. Machine learning-derived segmentation analysis is a step forward in the quantitative understanding of each phase in the time series 3D microtomography images.

CRediT authorship contribution statement

Ke Xu: Conceptualization, Methodology, μCT experiments, Software, Data Curation, Visualization, Writing - Original draft, Writing - Review & Editing.

Qingxu Jin: Software, Methodology, Investigation, Data Curation, Visualization, Writing - Original Draft, Writing - Review & Editing.

Jiaqi Li: Methodology, Writing - Review & Editing.

Daniela M. Ushizima: Software, Writing - Review & Editing.

Victor C. Li: Project administration, Methodology, Writing - Review & Editing, Funding acquisition.

Kimberly E. Kurtis: Supervision, Writing - Review & Editing, Funding acquisition.

Paulo J. M. Monteiro: Conceptualization, Writing - Review & Editing, Supervision, Funding acquisition.

Declaration of competing interest

The authors declare the following financial interests/personal relationships which may be considered as potential competing interests: Co-author is the Editor of the Cement and Concrete Research - K.K.

Data availability

Data will be made available on request.

Acknowledgments

This work was supported by the SusChEM program, Grant No. DMR-1410557, and the Division of Materials Research Ceramics Program, DMR-CER, Grant No. 1935604 of National Science Foundation. The authors are grateful for the funding support by the U.S. Department of Energy ARPA-e (award No. DE-AR0001141) to the University of Michigan. This research used resources (Beamline 8.3.2) of the Advanced Light Source, a U.S. DOE Office of Science User Facility under contract no. DE-AC02-05CH11231. The authors thank Dilworth Parkinson for assistance with the μCT experiments.

Appendix A. Supplementary data

Supplementary data to this article can be found online at https://doi.org/10.1016/j.cemconres.2023.107164.

References

[1] M.D. Lepech, V.C. Li, Long term durability performance of engineered cementitious composites/Langzeitbeständigkeit systematisch entwickelter zusammengesetzter zement gebundener werkstoffe, Restor. Build. Monuments 12 (2006) 119–132.
[2] P.K. Mehta, Sustainable cements and concrete for the climate change era–a review, in: Proceedings of the Second International Conference on Sustainable Construction Materials and Technologies, Aneona, Italy, Citeseer, 2010, pp. 28–30.
[3] P.J. Monteiro, S.A. Miller, A. Horvath, Towards sustainable concrete, Nat. Mater. 16 (2017) 698–699.
[4] V.C. Li, On engineered cementitious composites (ECC) a review of the material and its applications, J. Adv. Concr. Technol. 1 (2003) 215–230.
[5] V.C. Li, Engineered Cementitious Composites (ECC) Material, Structural, and Durability Performance, 2008.
[6] V.C. Li, Reflections on the Research and Development of Engineered Cementitious Composites (ECC), 2002.
[7] V.C. Li, Engineered Cementitious Composites (ECC): Bendable Concrete for Sustainable and Resilient Infrastructure, Springer, 2019.
[8] Q. Jin, V.C. Li, Development of lightweight engineered cementitious composite for durability enhancement of tall concrete wind towers, Cem. Concr. Compos. 96 (2019) 87–94.
[9] Q. Jin, V.C. Li, Structural and durability assessment of ECC/concrete dual-layer system for tall wind turbine towers, Eng. Struct. 196 (2019), 109338.
[10] Q. Jin, C.K. Leung, Fiber reinforced cementitious composites (FRCC) plate for the anchoring of FRP sheet on concrete member, in: Advances in FRP Composites in Civil Engineering, Springer, 2011, pp. 53–56.
[11] M.M. Islam, Q. Zhang, Q. Jin, A review of existing codes and standards on design factors for UHPC placement and fiber orientation, Constr. Build. Mater. 345 (2022), 128308.
[12] V.C. Li, Engineered Cementitious Composites (ECC)-tailored Composites Through Micromechanical Modeling, 1998.
[13] C. Lu, C.K. Leung, V.C. Li, Numerical model on the stress field and multiple cracking behavior of engineered cementitious composites (ECC), Constr. Build. Mater. 133 (2017) 118–127.
[14] V.C. Li, in: Micromechanics and Engineered Cementitious Composites (ECC) Design Basis, Engineered Cementitious Composites (ECC), Springer, 2019, pp. 11–71.
[15] E.-H. Yang, S. Wang, Y. Yang, V.C. Li, Fiber-bridging constitutive law of engineered cementitious composites, J. Adv. Concr. Technol. 6 (2008) 181–193.
[16] R. Ranade, M. Stults, B. Lee, V. Li, Effects of fiber dispersion and flaw size distribution on the composite properties of PVA-ECC, in: High Performance Fiber Reinforced Cement Composites 6, Springer, 2012, pp. 107–114.
[17] K. Tosun-Felekoğlu, B. Felekoğlu, R. Ranade, B.Y. Lee, V.C. Li, The role of flaw size and fiber distribution on tensile ductility of PVA-ECC, Compos. Part B 56 (2014) 536–545.
[18] S. Fan, M. Li, X-ray computed microtomography of three-dimensional microcracks and self-healing in engineered cementitious composites, Smart Mater. Struct. 24 (2014), 015021.
[19] Q. Qiu, J. Zhu, J.-G. Dai, In-situ X-ray microcomputed tomography monitoring of steel corrosion in engineered cementitious composite (ECC), Constr. Build. Mater. 262 (2020), 120844.
[20] C. Lu, V.C. Li, C.K. Leung, Flaw characterization and correlation with cracking strength in Engineered Cementitious Composites (ECC), Cem. Concr. Res. 107 (2018) 64–74.
[21] A.R. Sakulich, V.C. Li, Nanoscale characterization of engineered cementitious composites (ECC), Cem. Concr. Res. 41 (2011) 169–175.
[22] F. Liu, K. Xu, W. Ding, Y. Qiao, L. Wang, Microstructural characteristics and their impact on mechanical properties of steel-PVA fiber reinforced concrete, Cem. Concr. Compos. 123 (2021), 104196.
[23] K. Xu, A.S. Tremsin, J. Li, D.M. Ushizima, C.A. Davy, A. Bouterf, Y.T. Su, M. Marroccoli, A.M. Mauro, M. Osanna, A. Telesca, P.J.M. Monteiro, Microstructure and water absorption of ancient concrete from Pompeii: an integrated synchrotron microtomography and neutron radiography characterization, Cem. Concr. Res. 139 (2021).
[24] S. Brisard, M. Serdar, P.J. Monteiro, Multiscale X-ray tomography of cementitious materials: a review, Cem. Concr. Res. 128 (2020), 105824.
[25] R. Lorenzoni, I. Curosu, F. Léonard, S. Paciornik, V. Mechtcherine, F.A. Silva, G. Bruno, Combined mechanical and 3D-microstructural analysis of strain-hardening cement-based composites (SHCC) by in-situ X-ray microtomography, Cem. Concr. Res. 136 (2020), 106139.

[26] R. Lorenzoni, I. Curosu, S. Paciornik, V. Mechtcherine, M. Oppermann, F. Silva, Semantic segmentation of the micro-structure of strain-hardening cement-based composites (SHCC) by applying deep learning on micro-computed tomography scans, Cem. Concr. Compos. 108 (2020), 103551.
[27] D. Ushizima, K. Xu, P.J. Monteiro, Materials data science for microstructural characterization of archaeological concrete, MRS Adv. 5 (2020) 305–318.
[28] D. Zhang Y. Zhang A. Dasari K.H. Tan Y. Weng, Effect of spatial distribution of polymer fibers on preventing spalling of UHPC at high temperatures, Cem. Concr. Res., 140 106281.
[29] D.Y. Parkinson, D.M. Pelt, T. Perciano, D. Ushizima, H. Krishnan, H.S. Barnard, A. A. MacDowell, J. Sethian, Machine learning for micro-tomography, developments in X-ray tomography XI, SPIE (2017) 85–92.
[30] A. Fioravante de Siqueira, D.M. Ushizima, S.J. van der Walt, A reusable neural network pipeline for unidirectional fiber segmentation, Sci. Data 9 (2022) 1–14.
[31] A. Badran, D. Parkinson, D. Ushizima, D. Marshall, E. Maillet, Validation of deep learning segmentation of CT images of fiber-reinforced composites, J. Compos. Sci. 6 (2022) 60.
[32] Y. Dong, C. Su, P. Qiao, L. Sun, Microstructural crack segmentation of three-dimensional concrete images based on deep convolutional neural networks, Constr. Build. Mater. 253 (2020), 119185.
[33] O. Ronneberger, P. Fischer, T. Brox, U-net: convolutional networks for biomedical image segmentation, in: International Conference on Medical Image Computing and Computer-assisted Intervention, Springer, 2015, pp. 234–241.
[34] N. Siddique, S. Paheding, C.P. Elkin, V. Devabhaktuni, U-net and its variants for medical image segmentation: a review of theory and applications, IEEE Access 9 (2021) 82031–82057.
[35] M. Li, V.C. Li, Rheology, fiber dispersion, and robust properties of engineered cementitious composites, Mater. Struct. 46 (2013) 405–420.
[36] W. Si, M. Cao, L. Li, Establishment of fiber factor for rheological and mechanical performance of polyvinyl alcohol (PVA) fiber reinforced mortar, Constr. Build. Mater. 265 (2020), 120347.
[37] M. Cao, W. Si, C. Xie, Relationship of rheology, fiber dispersion, and strengths of polyvinyl alcohol fiber-reinforced cementitious composites, ACI Mater. J. 117 (2020) 191–204.
[38] Y. Ding, J.-P. Liu, Y.-L. Bai, Linkage of multi-scale performances of nano-CaCO3 modified ultra-high performance engineered cementitious composites (UHP-ECC), Constr. Build. Mater. 234 (2020), 117418.
[39] B. Zhu, J. Pan, J. Li, P. Wang, M. Zhang, Relationship between microstructure and strain-hardening behaviour of 3D printed engineered cementitious composites, Cem. Concr. Compos. 133 (2022) 1–23, 104677.
[40] W. Nguyen, D. Hernández-Cruz, K. Celik, J.F. Duncan, P.J. Monteiro, C.P. Ostertag, In-situ tensile and corrosion damage characterization of fiber-reinforced cementitious composites using X-ray micro-computed tomography, in: The 9th International Conference on Fracture Mechanics of Concrete and Concrete structures, 2016.
[41] A. MacDowell, D. Parkinson, A. Haboub, E. Schaible, J. Nasiatka, C. Yee, J. Jameson, J. Ajo-Franklin, C. Brodersen, A. McElrone, X-ray micro-tomography at the advanced light source, developments in X-ray tomography VIII, Int. Soc. Opt. Photonics 8506 (2012) 298–311.
[42] D. Gürsoy, F. De Carlo, X. Xiao, C. Jacobsen, TomoPy: a framework for the analysis of synchrotron tomographic data, J. Synchrotron Radiat. 21 (2014) 1188–1193.
[43] J. Li, W. Zhang, K. Xu, P.J. Monteiro, Fibrillar calcium silicate hydrate seeds from hydrated tricalcium silicate lower cement demand, Cem. Concr. Res. 137 (2020), 106195.
[44] D. Ushizima, D. Parkinson, P. Nico, J. Ajo-Franklin, A. MacDowell, B. Kocar, W. Bethel, J. Sethian, Statistical segmentation and porosity quantification of 3d x-ray microtomography, in: Applications of Digital Image Processing XXXIV, International Society for Optics and Photonics, 2011, p. 813502.
[45] J. Schindelin, I. Arganda-Carreras, E. Frise, V. Kaynig, M. Longair, T. Pietzsch, S. Preibisch, C. Rueden, S. Saalfeld, B. Schmid, Fiji: an open-source platform for biological-image analysis, Nat. Methods 9 (2012) 676–682.
[46] B.D. Levin, Y. Jiang, E. Padgett, S. Waldon, C. Quammen, C. Harris, U. Ayachit, M. Hanwell, P. Ercius, D.A. Muller, Tutorial on the visualization of volumetric data using tomviz, Microsc. Today 26 (2018) 12–17.
[47] P. Viseshchitra, P. Ercius, P.J. Monteiro, M. Scott, D. Ushizima, J. Li, K. Xu, H. R. Wenk, 3D nanotomography of calcium silicate hydrates by transmission electron microscopy, J. Am. Ceram. Soc. 104 (2021) 1852–1862.
[48] S. Chauhan, W. Rühaak, H. Anbergen, A. Kabdenov, M. Freise, T. Wille, I. Sass, Phase segmentation of X-ray computer tomography rock images using machine learning techniques: an accuracy and performance study, Solid Earth 7 (2016).
[49] C.S. Lee, A.J. Tyring, N.P. Deruyter, Y. Wu, A. Rokem, A.Y. Lee, Deep-learning based, automated segmentation of macular edema in optical coherence tomography, Biomed. Opt. Express 8 (2017) 3440–3448.
[50] I. Arganda-Carreras, V. Kaynig, C. Rueden, K.W. Eliceiri, J. Schindelin, A. Cardona, H. Sebastian Seung, Trainable weka segmentation: a machine learning tool for microscopy pixel classification, Bioinformatics 33 (2017) 2424–2426.
[51] D. Ushizima K. Xu P.J. Monteiro, Materials data science for microstructural characterization of archaeological concrete, MRS Adv., 1-14.
[52] Ö.F. Arar, K. Ayan, A feature dependent naive bayes approach and its application to the software defect prediction problem, Appl. Soft Comput. 59 (2017) 197–209.
[53] F. Alam, S. Pachauri, Detection using weka, in: Advances in Computational Sciences and Technology 10, 2017, pp. 1731–1743.
[54] G.H. John, P. Langley, Estimating Continuous Distributions in Bayesian Classifiers, arXiv preprint arXiv:1302.4964, 2013.
[55] S. Area, R. Mesra, Analysis of Bayes, Neural Network and Tree Classifier of Classification Technique in Data Mining Using WEKA, 2012.
[56] W. Buntine, Theory refinement on Bayesian networks, in: Uncertainty Proceedings 1991, Elsevier, 1991, pp. 52–60.
[57] D. Grossman, P. Domingos, Learning Bayesian network classifiers by maximizing conditional likelihood, in: Proceedings of the Twenty-first International Conference on Machine Learning, 2004, p. 46.
[58] M.W. Gardner, S. Dorling, Artificial neural networks (the multilayer perceptron)—a review of applications in the atmospheric sciences, Atmos. Environ. 32 (1998) 2627–2636.
[59] T. Hegazy, P. Fazio, O. Moselhi, Developing practical neural network applications using back-propagation, Comput. Aided Civ. Inf. Eng. 9 (1994) 145–159.
[60] P.E. Utgoff, Incremental induction of decision trees, Mach. Learn. 4 (1989) 161–186.
[61] S. Choudhury, A. Bhowal, Comparative analysis of machine learning algorithms along with classifiers for network intrusion detection, in: 2015 International Conference on Smart Technologies and Management for Computing, Communication, Controls, Energy and Materials (ICSTM), IEEE, 2015, pp. 89–95.
[62] N. Landwehr, M. Hall, E. Frank, Logistic model trees, Mach. Learn. 59 (2005) 161–205.
[63] J. Friedman, T. Hastie, R. Tibshirani, Additive logistic regression: a statistical view of boosting (with discussion and a rejoinder by the authors), Ann. Stat. 28 (2000) 337–407.
[64] T.K. Ho, Random decision forests, in: Proceedings of 3rd International Conference on Document Analysis and Recognition, IEEE, 1995, pp. 278–282.
[65] R. Caruana, N. Karampatziakis, A. Yessenalina, An empirical evaluation of supervised learning in high dimensions, in: Proceedings of the 25th International Conference on Machine learning, 2008, pp. 96–103.
[66] H. Kervadec, J. Bouchtiba, C. Desrosiers, E. Granger, J. Dolz, I.B. Ayed, Boundary loss for highly unbalanced segmentation, in: International Conference on Medical Imaging With Deep Learning, PMLR, 2019, pp. 285–296.
[67] L. Yu, H. Chen, Q. Dou, J. Qin, P.-A. Heng, Automated melanoma recognition in dermoscopy images via very deep residual networks, IEEE Trans. Med. Imaging 36 (2016) 994–1004.
[68] G. Jurman, S. Riccadonna, C. Furlanello, A comparison of MCC and CEN error measures in multi-class prediction, PloS one 7 (2012), e41882.
[69] D.M. Powers, Evaluation: From Precision, Recall and F-measure to ROC, Informedness, Markedness and Correlation, 2011.
[70] L. Bi, J. Kim, E. Ahn, A. Kumar, M. Fulham, D. Feng, Dermoscopic image segmentation via multistage fully convolutional networks, IEEE Trans. Biomed. Eng. 64 (2017) 2065–2074.
[71] M. Hall, E. Frank, G. Holmes, B. Pfahringer, P. Reutemann, I.H. Witten, The WEKA data mining software: an update, ACM SIGKDD Explor. Newsl. 11 (2009) 10–18.
[72] N. Bossa, P. Chaurand, J. Vicente, D. Borschneck, C. Levard, O. Aguerre-Chariol, J. Rose, Micro-and nano-X-ray computed-tomography: a step forward in the characterization of the pore network of a leached cement paste, Cem. Concr. Res. 67 (2015) 138–147.
[73] T. Sugiyama, M. Promentilla, T. Hitomi, N. Takeda, Application of synchrotron microtomography for pore structure characterization of deteriorated cementitious materials due to leaching, Cem. Concr. Res. 40 (2010) 1265–1270.
[74] B.K. Bay, T.S. Smith, D.P. Fyhrie, M. Saad, Digital volume correlation: three-dimensional strain mapping using X-ray tomography, Exp. Mech. 39 (1999) 217–226.
[75] C.J. Brandon, R.L. Hohlfelder, M.D. Jackson, J.P. Oleson, Building for Eternity: The History and Technology of Roman Concrete Engineering in the Sea, Oxbow books, 2014.
[76] B.K. Bay, Methods and applications of digital volume correlation, J. Strain Anal. Eng. Des. 43 (2008) 745–760.
[77] M. Palanca, A.J. Bodey, M. Giorgi, M. Viceconti, D. Lacroix, L. Cristofolini, E. Dall'Ara, Local displacement and strain uncertainties in different bone types by digital volume correlation of synchrotron microtomograms, J. Biomech. 58 (2017) 27–36.
[78] A. Bouterf, J. Adrien, E. Maire, X. Brajer, F. Hild, S. Roux, Failure mechanisms of plasterboard in nail pull test determined by x-ray microtomography and digital volume correlation, Exp. Mech. 56 (2016) 1427–1437.
[79] A. Bouterf, S. Roux, F. Hild, J. Adrien, E. Maire, S. Meille, Digital volume correlation applied to X-ray tomography images from spherical indentation tests on lightweight gypsum, Strain 50 (2014) 444–453.
[80] S. Roux, F. Hild, P. Viot, D. Bernard, Three-dimensional image correlation from X-ray computed tomography of solid foam, Compos. A: Appl. Sci. Manuf. 39 (2008) 1253–1265.
[81] H. Leclerc, J.-N. Périé, F. Hild, S. Roux, Digital volume correlation: what are the limits to the spatial resolution? Mech. Ind. 13 (2012) 361–371.
[82] T. Taillandier-Thomas, S. Roux, T.F. Morgeneyer, F. Hild, Localized strain field measurement on laminography data with mechanical regularization, Nucl. Instrum. Methods Phys. Res., Sect. B 324 (2014) 70–79.
[83] B. Xu, Z. Li, Performance of novel thermal energy storage engineered cementitious composites incorporating a paraffin/diatomite composite phase change material, Appl. Energy 121 (2014) 114–122.
[84] K. Yu, Y. Wang, J. Yu, S. Xu, A strain-hardening cementitious composites with the tensile capacity up to 8%, Constr. Build. Mater. 137 (2017) 410–419.
[85] V.C. Li, Tailoring ECC for special attributes: a review, Int. J. Concr. Struct. Mater. 6 (2012) 135–144.
[86] M.D. Lepech, V.C. Li, Water Permeability of Cracked Cementitious Composites, 2005.
[87] D. Zhang, B. Jaworska, H. Zhu, K. Dahlquist, V.C. Li, Engineered cementitious composites (ECC) with limestone calcined clay cement (LC3), Cem. Concr. Compos. 114 (2020), 103766.

[88] D. Zhang, H. Zhu, M. Hou, K.E. Kurtis, P.J. Monteiro, V.C. Li, Optimization of matrix viscosity improves polypropylene fiber dispersion and properties of engineered cementitious composites, Constr. Build. Mater. 346 (2022), 128459.
[89] M.J. Matthewson, C.R. Kurkjian, S.T. Gulati, Strength measurement of optical fibers by bending, J. Am. Ceram. Soc. 69 (1986) 815–821.
[90] Z. Lin, T. Kanda, V.C. Li, On Interface Property Characterization and Performance of Fiber Reinforced Cementitious Composites, 1999.
[91] O. Stamati, E. Roubin, E. Andò, Y. Malecot, P. Charrier, Fracturing process of micro-concrete under uniaxial and triaxial compression: insights from in-situ X-ray mechanical tests, Cem. Concr. Res. 149 (2021), 106578.